BIO Ice-Ocean and Wave Forecasting Models and Systems for Eastern Canadian Waters

C.L. Tang, T. Yao, W. Perrie, B.M Detracey, B. Toulany, E. Dunlap, Y. Wu

Ocean Sciences Division
Maritimes Region
Fisheries and Oceans Canada

Bedford Institute of Oceanography
P.O. Box 1006
Dartmouth, Nova Scotia
Canada B2Y 4A2

2008

Canadian Technical Report of Hydrography and Ocean Sciences 261

Fisheries and Oceans Canada | Pêches et Océans Canada

Canada

Canadian Technical Report of Hydrography and Ocean Sciences

Technical reports contain scientific and technical information of a type that represents a contribution to existing knowledge but which is not normally found in the primary literature. The subject matter is generally related to programs and interests of the Oceans and Science sectors of Fisheries and Oceans Canada.

Technical reports may be cited as full publications. The correct citation appears above the abstract of each report. Each report is abstracted in the data base *Aquatic Sciences and Fisheries Abstracts*.

Technical reports are produced regionally but are numbered nationally. Requests for individual reports will be filled by the issuing establishment listed on the front cover and title page.

Regional and headquarters establishments of Ocean Science and Surveys ceased publication of their various report series as of December 1981. A complete listing of these publications and the last number issued under each title are published in the *Canadian Journal of Fisheries and Aquatic Sciences*, Volume 38: Index to Publications 1981. The current series began with Report Number 1 in January 1982.

Rapport technique canadien sur l'hydrographie et les sciences océaniques

Les rapports techniques contiennent des renseignements scientifiques et techniques qui constituent une contribution aux connaissances actuelles mais que l'on ne trouve pas normalement dans les revues scientifiques. Le sujet est généralement rattaché aux programmes et intérêts des secteurs des Océans et des Sciences de Pêches et Océans Canada.

Les rapports techniques peuvent être cités comme des publications à part entière. Le titre exact figure au-dessus du résumé de chaque rapport. Les rapports techniques sont résumés dans la base de données *Résumés des sciences aquatiques et halieutiques*.

Les rapports techniques sont produits à l'échelon régional, mais numérotés à l'échelon national. Les demandes de rapports seront satisfaites par l'établissement auteur dont le nom figure sur la couverture et la page de titre.

Les établissements de l'ancien secteur des Sciences et Levés océaniques dans les régions et à l'administration centrale ont cessé de publier leurs diverses séries de rapports en décembre 1981. Vous trouverez dans l'index des publications du volume 38 du *Journal canadien des sciences halieutiques et aquatiques*, la liste de ces publications ainsi que le dernier numéro paru dans chaque catégorie. La nouvelle série a commencé avec la publication du rapport numéro 1 en janvier 1982.

Canadian Technical Report of

Hydrography and Ocean Science No. 261

2008

BIO Ice-Ocean and Wave Forecasting Models and Systems for Eastern Canadian Waters

by

C.L. Tang, T. Yao, W. Perrie. B.M. Detracey, B. Toulany, E. Dunlap, Y. Wu

Ocean Sciences Division
Maritimes Region
Fisheries and Oceans Canada

Bedford Institute of Oceanography
1 Challenger Drive
Dartmouth, Nova Scotia
Canada B2Y 4A2

ACKNOWLEDGEMENTS

The research documented in this report has been supported by Program of Energy Research and Development, Canadian Coast Guard New Initiative Fund (CCG NIF), Canadian Foundation for Climate and Atmospheric Sciences (CFCAS) and other funding agencies. The meteorological and sea-ice data are provided by Canadian Meteorological Centre and Canadian Ice Service (CIS), respectively. Many people helped and were involved in the work, either directly or indirectly. Peter Smith initiated the programs that led to the application and implementation of Princeton Ocean Model and WaveWatch III . Simon Prinsenberg, John Loder and Charles Hannah assisted in data acquisition and facilitated funding of the project. Guoqi Han at NWAFC (Northwest Atlantic fisheries Centre, DFO) provided tidal constants from his ocean tide model. Doug Bancroft, Tom Carrieres, Hai Tran at CIS and Alain Caya at Meteorological Service of Canada assisted in the transfer of CECOM to CIS and participated in ice model validation. Brian Stone, Étienne Beaule, Ron Dawson, Katherine MacIntyre and Jean Maillette at Canadian Coast Guard managed the CCG NIF project, assisted in field trials and transfer of the model output to CANSARP (Canadian Search and Rescue Planning).

© Her Majesty the Queen in Right of Canada, 2008
Cat. No: FS 97-18/261E ISSN: 0711-6764

Correct citation for this publication:

Tang, C.L., T. Yao, W. Perrie. B.M. Detracey, B. Toulany, E. Dunlap, Y. Wu, 2008. BIO Ice-Ocean and Wave Forecasting Models and Systems for Eastern Canadian Waters. Can. Tech. Rep. Hydrogr. Ocean Sci. No. 261: iv + 61 pp.

TABLE OF CONTENTS

Page

Acknowledgements ii

Table of contents iii

Abstract/Résumé iv

1. Introduction 1

2. Governing equations of ocean and ice models 1
   2.1 Princeton Ocean Model (POM)
   2.2 Ice dynamics
   2.3 Multiple ice categories
   2.4 Ice thermodynamics

3. Finite difference implementation 17
   3.1 POM
   3.2 Ice dynamics
   3.3 Mechanical redistribution of ice

4. Canadian East Coast Ocean Model (CECOM) 24
   4.1 Rotated spherical coordinates
   4.2 The CECOM domain
   4.3 Ocean initial state, boundary conditions and model spin-up
   4.4 Ice categories

5. Model physics of WaveWatch III (WW3) 32

6. The Bedford Institute Ocean Forecasting System (BIOFS) 33
   6.1 Input data
   6.2 Data assimilation in CECOM
   6.3 Operational implementation of CECOM
   6.4 Operational implementation of WW3

References 50

Appendix 1. Turbulence closure 55
Appendix 2. Generalised sigma coordinates 56
Appendix 3. Rotated spherical coordinates 58
Appendix 4. Two-dimensional statistical interpolation 60

ABSTRACT

Tang, C.L., T. Yao, W. Perrie. B.M. Detracey, B. Toulany, E. Dunlap, Y. Wu, 2008. BIO Ice-Ocean and Wave Forecasting Models and System for Eastern Canadian Waters. Can. Tech. Rep. Hydrogr. Ocean Sci. No. 261: iv + 61 pp.

The ice-ocean and wave models used in the Bedford Institute Ocean Forecasting System (BIOFS) are described. The coupled ice-ocean model, Canadian East Coast Ocean Model (CECOM), is a based on the Princeton Ocean Model and a multicategory ice model. The wave model is WaveWatch III (WW3) developed by the U.S. Navy. The governing equations, model domains, numerical grids, coordinate system, finite difference scheme, forcing data, boundary conditions for each of the models are explained. The models are implemented in BIOFS and run in real-time to provide 48-hour forecasts of ocean and wave conditions for eastern Canadian waters. BIOFS includes a procedure to assimilate sea ice and sea surface temperature data into CECOM. The structure and operations of BIOFS, and the methods of data assimilation are described.

RÉSUMÉ

Nous décrivons les modèles glace-océan et les modèles de vagues utilisés dans le système de prévision océanique de l'Institut océanographique de Bedford (Bedford Institute Ocean Forecasting System, BIOFS). Le modèle CECOM (Canadian East Coast Ocean Model) est le modèle couplé glace-océan de la côte Est du Canada, basé sur le modèle océanique de Princeton et sur un modèle multicatégorie des glaces. Le modèle WaveWatch III (WW3) est le modèle des vagues mis au point par les Forces navales des États-Unis. Nous expliquons les équations principales, les domaines des modèles, les grilles numériques, le système de coordonnées, le schéma de différences finies, les données de forçage, ainsi que les conditions limites. Les modèles sont appliqués au BIOFS et sont utilisés en temps réel pour fournir des prévisions sur 48 heures des conditions océaniques et de l'état des vagues dans les eaux de l'Est du Canada. Le BIOFS comprend une procédure permettant d'assimiler dans le CECOM des données sur les glaces de mer et sur la température à la surface de la mer. Nous décrivons en outre la structure et les opérations du BIOFS, de même que les méthodes d'assimilation des données.

1. Introduction

Ocean forecast research at BIO (Bedford Institute of Oceanography) started in the early 1990s when ice and wave models were developed under a series of PERD (Program for Energy Research and Development) projects. In the mid-1990, a coupled ice-ocean model (Tang et al., 1996a,b) and a second generation wave model (Perrie et al., 1989) were implemented in a real-time forecasting system at BIO to provide daily forecasts of ice and waves for eastern Canadian waters. The ocean component of the coupled ice-model is a linear diagnostic ocean model and the ice component is the Hibler (1979) two-category ice model. In 1998, the coupled ice-ocean model was replaced by a coupled multi-category sea ice model and the Princeton Ocean Model (CIOM, Coupled Ice-Ocean Model) (Yao et al., 2000; Yao and Tang, 2003; Tang et al., 2004; Dunlap et al., 2007). This model was also used by Canadian Ice Service for operational ice forecasting.

A new effort was initiated in the mid-2000 to improve the forecast models. The model domain of CIOM, which covers the Labrador Sea and the Grand Banks, was extended north to include Baffin Bay and south to include the Scotian Shelf and the Gulf of St. Lawrence. The latest POM codes were adopted to improve the model physics and computational efficiency. The generalized sigma coordinate and the rotated spherical coordinate systems were employed to improve the vertical and horizontal resolution. The modified model, Canadian East Coast Ocean Model (CECOM), was implemented in a new forecasting system in September 2008. The associated wave forecasts were also upgraded and are now produced by an advanced third generation wave model, WaveWatch 3 (WW3). The wave forecasts are produced for WW3 implemented on a system of nested grids consisting of coarse resolution (1.0^{o}) for the entire Atlantic, intermediate resolution (0.5^{o}) for the Northwest Atlantic and fine resolution (10') for Atlantic Canada waters including the Grand Banks and Scotian Shelf.

The purpose of this report is to document the progress made in the ocean forecasting models. Upgrading, calibration and validation of the models are carried out on an ongoing basis as improved parameterization of ocean processes, numerics and algorithm, and new data become available. The report provides a general description of CECOM, WW3 and the forecasting systems that integrate the operations of data input/output, model execution and display of forecast results. The systems are run unattended and produce ocean, ice and wave forecasts for eastern Canadian waters twice a day. Selected forecasts including surface trajectories, ice concentration, wave height and direction, and sea surface elevation are displayed in graphic forms at the following BIO website:

http://www.mar.dfo-mpo.gc.ca/science/ocean/icemodel/ice_ocean_forecast.html

2. Governing Equations of Ocean and Ice Models

The ocean component of the coupled ice-ocean model used in the ocean forecasting system is the Princeton Ocean Model (Blumberg and Mellor, 1987). A user's guide can be obtained from the POM website, http://www.aos.princeton.edu/wwwpublic/htdocs.pom/. The

ice component is a multi-category ice model based on the formulation of Thorndike et al (1975), Hibler (1980) and Flato (1994). In the following sections, we outline the governing equations, the finite difference scheme and the implementation for eastern Canadian waters.

2.1 Princeton Ocean Model (POM)

The Princeton Ocean Model is a widely used model for modeling of coastal and open oceans. It is a free surface, primitive equation, terrain-following model with an imbedded turbulence closure model. It was developed by Blumberg and Mellor (1987) in the late 1970s with subsequent contributions by others.

Dynamic and Thermodynamic Equations

Consider a Cartesian (x, y, z) coordinate system with velocity components (u, v, w), the ocean bottom at $z = -H$ and a free surface at $z = \eta$. The continuity equation is

$$\frac{\partial u}{\partial x}+\frac{\partial v}{\partial y}+\frac{\partial w}{\partial z}=0. \tag{2.1}$$

The momentum equations are

$$\frac{\partial u}{\partial t}+u\frac{\partial u}{\partial x}+v\frac{\partial u}{\partial y}+w\frac{\partial u}{\partial z}-fv=-\frac{1}{\rho_o}\frac{\partial p}{\partial x}+\frac{\partial}{\partial z}\left(K_M\frac{\partial u}{\partial z}\right)+M_x \tag{2.2}$$

$$\frac{\partial v}{\partial t}+u\frac{\partial v}{\partial x}+v\frac{\partial v}{\partial y}+w\frac{\partial v}{\partial z}+fu=-\frac{1}{\rho_o}\frac{\partial p}{\partial y}+\frac{\partial}{\partial z}\left(K_M\frac{\partial v}{\partial z}\right)+M_y \tag{2.3}$$

$$\rho g=-\frac{\partial p}{\partial z} \tag{2.4}$$

where f is the Coriolis parameter, g is the acceleration of gravity, K_M is a vertical eddy diffusivity, and M_x, M_y are horizontal mixing terms. The hydrostatic and Boussinesq approximations are made. ρ_o is a reference density and ρ is the in situ density. Pressure p at depth z from (2.4) is

$$p=p_{atm}+g\int_{z}^{\eta}\rho dz$$

where p_{atm} is the atmospheric pressure.

The conservation of heat and salt for potential temperature T and salinity S are

$$\frac{\partial T}{\partial t}+u\frac{\partial T}{\partial x}+v\frac{\partial T}{\partial y}+w\frac{\partial T}{\partial z}=\frac{\partial}{\partial z}\left(K_H\frac{\partial T}{\partial z}\right)+\nabla\cdot(A_H\nabla T)-\frac{1-A}{\rho_0 c_p}\frac{\partial I}{\partial z} \tag{2.5}$$

$$\frac{\partial S}{\partial t}+u\frac{\partial S}{\partial x}+v\frac{\partial S}{\partial y}+w\frac{\partial S}{\partial z}=\frac{\partial}{\partial z}\left(K_H\frac{\partial S}{\partial z}\right)+\nabla\cdot(A_H\nabla S) \tag{2.6}$$

where K_H and A_H are the vertical and horizontal diffusivities respectively for heat and salt. A is ice concentration. I is the shortwave radiation (Paulson and Simpson, 1977):

$$I=-(1-\alpha_w)Q\left[R\exp(z/\xi_1)+(1-R)\exp(z/\xi_2)\right] \tag{2.7}$$

where Q is the shortwave radiation reaching the sea surface, α_w is the albedo for water, ξ_1 and ξ_2 are the attenuation depths of the red and blue-green spectral components of the shortwave radiation. Jerlov's (1968) values for water type IA, ξ_1 = 0.6 m, ξ_2 = 20 m, R = 0.62, are used here. Upward fluxes are defined positive. I is thus always negative. The last term of (2.5) states that no shortwave radiation can reach the ocean surface in fully ice covered waters.

The horizontal mixing terms in (2.2) and (2.3) are

$$M_x=\frac{\partial}{\partial x}\left(2A_M\frac{\partial u}{\partial x}\right)+\frac{\partial}{\partial y}\left[A_M\left(\frac{\partial u}{\partial y}+\frac{\partial v}{\partial x}\right)\right]$$

$$M_y=\frac{\partial}{\partial y}\left(2A_M\frac{\partial v}{\partial y}\right)+\frac{\partial}{\partial x}\left[A_M\left(\frac{\partial u}{\partial y}+\frac{\partial v}{\partial x}\right)\right] \tag{2.8}$$

A_M and A_H in (2.5), (2.6)and (2.8) are represented as Smagorinsky diffusivities

$$A_M=A_H=C\Delta x\Delta y\frac{1}{2}\left[\left(\frac{\partial u}{\partial x}\right)^2+\frac{1}{2}\left(\frac{\partial v}{\partial x}+\frac{\partial u}{\partial y}\right)^2+\left(\frac{\partial v}{\partial y}\right)^2\right]^{1/2}$$

where Δx and Δy are the grid intervals and C is a constant.

The vertical mixing coefficients K_M and K_H in (2.2) to (2.6) are computed from a second order turbulence closure (Appendix 1).

Surface and Bottom Boundary Conditions

The boundary conditions at the surface are

$$\rho_o K_M\left(\frac{\partial u}{\partial z},\frac{\partial v}{\partial z}\right)=\left(\tau_{0x},\tau_{0y}\right) \tag{2.9}$$

$$w=\frac{\partial\eta}{\partial t}+u\frac{\partial\eta}{\partial x}+v\frac{\partial\eta}{\partial y}$$

$$\rho_o K_H \left(\frac{\partial T}{\partial z}, \frac{\partial S}{\partial z} \right) = -\left(F_T / c_p, F_S \right) \tag{2.10}$$

where (τ_{0x}, τ_{0y}) is the surface wind stress, F_T is the heat flux, c_p is the specific heat of seawater and F_S is the salt flux. The bulk formulas to calculate the fluxes are given in Section 2.4.

The drag coefficient involved in the surface wind stress is based on the wind speed and stability (i.e. the difference between surface temperature and air temperature) tables (Smith, 1988). The surface fluxes of momentum, heat and salt in the presence of ice are described in Section 2.2 (Ice dynamics) and Section 2.4 (Ice thermodynamics).

The boundary conditions at the ocean bottom are

$$\rho_o K_M \left(\frac{\partial u}{\partial z}, \frac{\partial v}{\partial z} \right) = \left(\tau_{bx}, \tau_{by} \right) \tag{2.11}$$

$$w = -u \frac{\partial H}{\partial x} - v \frac{\partial H}{\partial y} \tag{2.12}$$

where (τ_{bx}, τ_{by}) is the bottom stress

$$\left(\tau_{bx}, \tau_{by} \right) = \rho_o C_D \left(u^2 + v^2 \right)^{1/2} (u, v). \tag{2.13}$$

The drag coefficient C_D is

$$C_D = \max \left\{ \left[\frac{1}{\kappa} \ln \left(\frac{H + z_b}{z_0} \right) \right]^{-2}, 2.5 \times 10^{-3} \right\} \tag{2.14}$$

where z_b is the z coordinate of the lowest grid point, at which (u,v) in (2.13) is evaluated, and z_0 is a roughness length. The maximum value is to account for cases when the bottom boundary layer is not resolved.

Generalised Sigma Coordinates

The more common applications of POM use sigma coordinates in the vertical

$$\sigma = \frac{z - \eta}{H + \eta}. \tag{2.15}$$

σ ranges from -1 at the bottom to 0 at the surface and varies linearly with z. Limitations to sigma coordinates appear in certain circumstances. For example, if high vertical resolution is desired in the near surface, sigma coordinates lead to a loss of resolution over the shelf break and

deep ocean. Generalised sigma coordinates, described by Mellor et al. (2002), remove the constraint of a linear variation of vertical coordinate with depth and include, as special cases, *z*-level as well as sigma coordinates. The momentum, temperature and salinity equations in generalised sigma coordinates are given in Appendix 2.

2.2 Ice Dynamics

The momentum balance governing ice velocity $\mathbf{u}_{ice} = (u_{ice}, v_{ice})$ is

$$m\frac{d\mathbf{u}_{ice}}{dt} + mf\,\mathbf{k}\times\mathbf{u}_{ice} = -mg\nabla\eta + A(\boldsymbol{\tau}_a - \boldsymbol{\tau}_w) + \mathbf{F} \tag{2.16}$$

where m is the mass per unit area, $\mathbf{k}$ is a unit vector in the upward direction, g is the acceleration of gravity, A is the ice concentration, $\boldsymbol{\tau}_a$ and $\boldsymbol{\tau}_w$ are the air and ocean stress and $\mathbf{F}$ is the force arising from gradients in internal ice stress. The present model neglects the inertial terms $d\mathbf{u}_{ice}/dt$.

The air and ocean stresses are parameterised as

$$\begin{aligned}\boldsymbol{\tau}_a &= \rho_a C_a |\mathbf{u}_a|\mathbf{u}_a \\ \boldsymbol{\tau}_w &= \rho_o C_w |\mathbf{u}_{ice} - \mathbf{u}|(\mathbf{u}_{ice} - \mathbf{u})\end{aligned} \tag{2.17}$$

where ρ_a and ρ_o are air and water densities, C_a and C_w are drag coefficients and $\mathbf{u}_a$ and $\mathbf{u}$ are surface winds and currents. Values for the constants and parameters are given in Table 2.1.

The stress of ice on the ocean (2.17) involves the ocean surface velocity. When solving for the ocean velocity we have found it is necessary to include the dependence of stress on ocean surface velocity (an implicit solution) rather than apply stress with the ocean velocity from the previous time step (an explicit solution).

Hibler (1979) models ice interaction as a viscous compressible fluid. The two-dimensional ice stress tensor σ_{ij} (i and j representing x and y in a Cartesian coordinate system) is

$$\sigma_{ij} = 2\tilde{\eta}\dot{\varepsilon}_{ij} + (\varsigma - \tilde{\eta})\dot{\varepsilon}_{kk}\delta_{ij} - \frac{1}{2}P\delta_{ij} \tag{2.18}$$

where $\dot{\varepsilon}_{ij}$ is the rate of strain, δ_{ij} is the Kronecker delta, ς and $\tilde{\eta}$ (functions of $\dot{\varepsilon}_{ij}$ and P) are bulk and shear viscosities and P is an ice pressure.

The ice force components in (2.16) are related to stress as

$$F_i = \frac{\partial\sigma_{ij}}{\partial x_j} \tag{2.19}$$

giving

$$F_x = \frac{\partial}{\partial x}\left[(\tilde{\eta}+\varsigma)\frac{\partial u_{ice}}{\partial x}+(\varsigma-\tilde{\eta})\frac{\partial v_{ice}}{\partial y}-\frac{P}{2}\right]+\frac{\partial}{\partial y}\left[\tilde{\eta}\left(\frac{\partial u_{ice}}{\partial y}+\frac{\partial v_{ice}}{\partial x}\right)\right] \tag{2.20}$$

$$F_y = \frac{\partial}{\partial y}\left[(\tilde{\eta}+\varsigma)\frac{\partial v_{ice}}{\partial y}+(\varsigma-\tilde{\eta})\frac{\partial u_{ice}}{\partial x}-\frac{P}{2}\right]+\frac{\partial}{\partial x}\left[\tilde{\eta}\left(\frac{\partial u_{ice}}{\partial y}+\frac{\partial v_{ice}}{\partial x}\right)\right].$$

Hibler (1979) selects the stress to lie on an ellipse in a principal axis system. The viscosities are

$$\varsigma = \frac{P}{2\Delta}, \quad \tilde{\eta} = \frac{P}{2\Delta e^2} \tag{2.21}$$

$$\Delta^2 = \left(\dot{\varepsilon}_{11}^2+\dot{\varepsilon}_{22}^2\right)\left(1+e^{-2}\right)+4e^{-2}\dot{\varepsilon}_{12}^2+2\dot{\varepsilon}_{11}\dot{\varepsilon}_{22}\left(1-e^{-2}\right)$$

where e is the ratio of ellipse axes.

The dependence of stress magnitude $\left(\sigma_{11}^2+\sigma_{22}^2\right)^{1/2}$ on $\dot{\varepsilon}_{ij}$ in a principal axis system is drawn in Figure 2.1. For isotropic divergence, $\dot{\varepsilon}_{11}=\dot{\varepsilon}_{22}$, $\dot{\varepsilon}_{11}+\dot{\varepsilon}_{22}>0$, the stress is zero. For isotropic convergence $\dot{\varepsilon}_{11}=\dot{\varepsilon}_{22}$, $\dot{\varepsilon}_{11}+\dot{\varepsilon}_{22}>0$, stress is a maximum. Stress is rate independent consistent with a plastic rheology.

The pressure P in (2.18) and (2.21) is related to mean ice thickness $\bar{h}$ and concentration A as

$$P = P^*\bar{h}\exp\left[-C(1-A)\right] \tag{2.22}$$

where P^* and C are parameters. An alternative parameterization of P derived from work done in ridging is given by Hibler (1980).

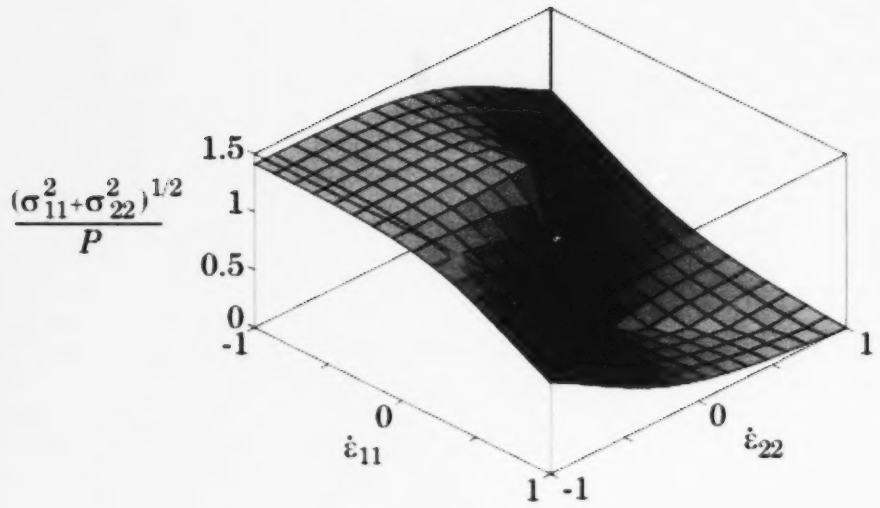

Figure 2.1. Dependence of stress magnitude on $\dot{\varepsilon}_{ij}$ in a principal axis system from (2.18) and (2.21).

2.3 Multiple Ice Categories

Thickness Distribution Function

The present work closely follows Hibler (1980). A thickness distribution function $g(h)$ is defined where $g(h)dh$ describes the fraction of area covered by ice of thickness between h and $h + dh$. Integrating $g(h)$ over all thickness results in

$$\int_0^\infty g(h)dh = 1. \tag{2.23}$$

In terms of $g(h)$, ice concentration is

$$A = \int_{0+}^{\infty} g(h)dh$$

where the integration is over non-zero h. Thickness $h = 0$ corresponds to open water. The presence of open water causes $g(h)$ to have a delta function behaviour at $h = 0$. The total ice volume per unit area or mean ice thickness, $\overline{h}$, is

$$\overline{h} = \int_0^\infty hg(h)dh . \tag{2.24}$$

The change in ice thickness is described by

$$\frac{\partial g}{\partial t} + \nabla \cdot (\mathbf{u}_{ice} g) + \frac{\partial (fg)}{\partial h} = \Psi + diffusion . \tag{2.25}$$

The second term in (2.25) represents the change in g from advection. The third term represents the change in g from ice growth or melt. $f(h)$ is the rate of change of ice thickness. The function Ψ represents mechanical redistribution of ice.

Mechanical Redistribution of Ice

The redistribution function Ψ satisfies two constraints. The first is obtained by integrating (2.25) over h,

$$\int_0^\infty \Psi dh = \nabla \cdot \mathbf{u}_{ice} . \tag{2.26}$$

(2.26) expresses a balance of ice area. During divergence of ice, the net flux of ice out of a region must be balanced by formation of open water. During convergence, ice must be redistributed from thinner to thicker ice categories to accommodate the influx. The second constraint is

$$\int_0^\infty h\Psi dh = 0 \tag{2.27}$$

which states that the redistribution process conserves ice volume.

Hibler (1980) proposes the redistribution function

$$\Psi(h,g) = \delta(h)\left[\frac{\sigma_{ij}\dot{\varepsilon}_{ij}}{P} + \dot{\varepsilon}_{ii}\right] + W_r(h,g)\frac{\sigma_{ij}\dot{\varepsilon}_{ij}}{P} \tag{2.28}$$

where $W_r(h,g)$ represents the ridging process. For Hibler's (1979) plastic rheology (2.21) we can write (2.28) as

$$\Psi(h,g) = \delta(h)\frac{1}{2}(\Delta + \dot{\varepsilon}_{ii}) + W_r(h,g)\frac{1}{2}(\Delta - \dot{\varepsilon}_{ii}). \tag{2.29}$$

To help visualise the behaviour of Ψ we have plotted the factors multiplying $\delta(h)$ and $W_r(h,g)$ in Figure 2.2. The factor $\frac{1}{2}(\Delta+\dot{\varepsilon}_{ii})$ determines the rate of open water formation. It is maximum for pure divergence and zero for convergence. The factor $\frac{1}{2}(\Delta-\dot{\varepsilon}_{ii})$ determines the rate of ridging. It is maximum for pure convergence and zero for divergence.

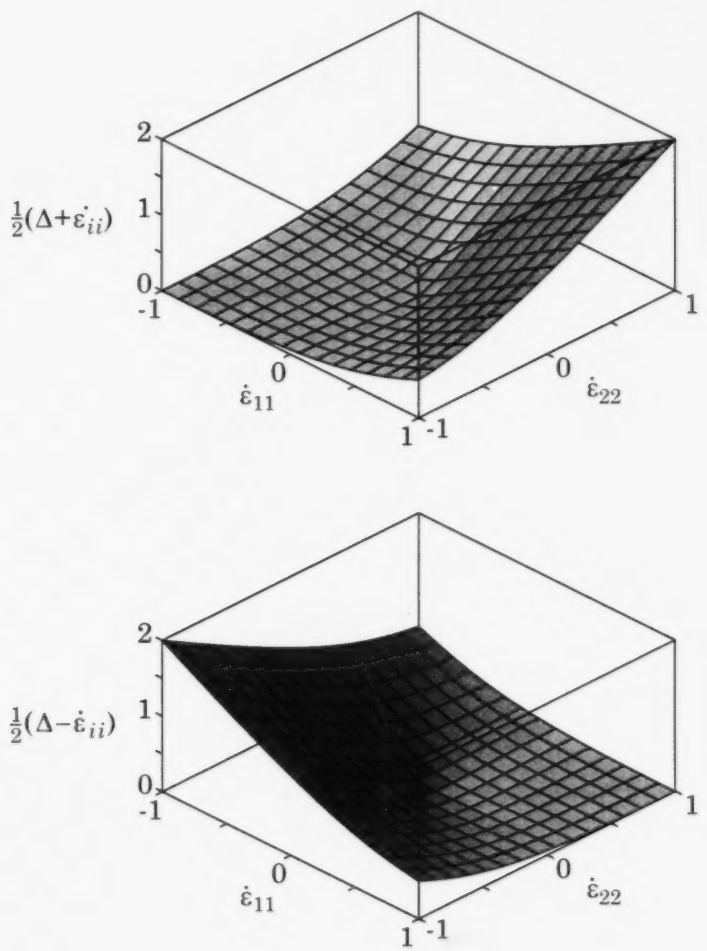

Figure 2.2. The factors $\frac{1}{2}(\Delta+\dot{\varepsilon}_{ii})$ and $\frac{1}{2}(\Delta-\dot{\varepsilon}_{ii})$ in the open water formation and ridging terms respectively of the ice redistribution function in a principal axis system.

Ice Ridging

The function W_r representing ridging in (2.28) is written in terms of thickness distribution functions $a(h)$ and $n(h)$ as

$$W_r(h,g) = \frac{-a(h)+n(h)}{\int[a(h)-n(h)]dh}. \tag{2.30}$$

The denominator in (2.30) ensures that the first constraint (2.26) is satisfied. $a(h)$ is the distribution of ice which undergoes ridging (the source). $n(h)$ is the distribution of the newly ridged ice (the destination). Thorndike et al. (1975) suggest $a(h)$ of the form

$$a(h) = b(h)g(h) \tag{2.31}$$

where $b(h)$ selectively weights thin ice for participation in the ridging. Thorndike et al. (1975) suggest $b(h)$ of the form

$$b(h) = \begin{cases} 1 - G(h)/G^* & 0 \le G(h) < G^* \\ 0 & G(h) > G^* \end{cases} \tag{2.32}$$

where $G(h)$ is the cumulative distribution function

$$G(h) = \int_0^h g(h')dh' \tag{2.33}$$

and G^* is a cutoff value. Ice from the thickness distribution above the cutoff does not contribute to the ridging.

The destination distribution $n(h)$ has the form of a convolution integral

$$n(h) = \int\gamma(h',h)a(h')dh \tag{2.34}$$

where $\gamma(h',h)$ represents the ice ridged from thickness h' to thickness h. In order that the second constraint (2.27) is satisfied we require

$$\int h\gamma(h',h)dh = h'. \tag{2.35}$$

We follow Thorndike et al. (1975) and take $\gamma(h',h)$ as

$$\gamma(h',h) = \frac{1}{k}\delta(h-kh') \tag{2.36}$$

which states that ice ridges to a multiple k of the original thickness. Note that (2.36) satisfies the constraint (2.35). An alternative form for $\gamma(h', h)$ is suggested by Hibler (1980).

Table 2.1. Parameters related to ice dynamics and redistribution

symbol	parameter	value
ρ_i	reference ice density (2.16)	910 kg m^{-3}
ρ_a	reference air density (2.17)	1.3 kg m^{-3}
ρ_o	reference water density (2.17)	1035 kg m^{-3}
C_a	air-ice drag coefficient (2.17)	3×10^{-3}
C_w	ice-water drag coefficient (2.17)	1.8×10^{-2}
e	ratio of ellipse axes (2.21)	2
P^*	ice strength parameter (2.22)	2.5×10^4 Pa
C	parameter in ice pressure (2.22)	20
G^*	cutoff for cumulative distribution function in ridging (2.32)	0.15
k	ratio of thickness in ridging (2.36)	15

2.4 Ice Thermodynamics

The coupled model is forced at the surface by atmospheric variables wind, air temperature, dew point temperature, cloudiness and precipitation. We first describe the parameterisations for heat fluxes. We then describe the surface heat balance and the thermodynamic coupling between ice and ocean.

Surface Heat Fluxes

Sensible Heat The upward flux of sensible heat H_S is given as

$$H_s = \rho_a c_{pa} c_H u_a (T_s - T_a) \tag{2.37}$$

where ρ_a is the density of air,
c_{pa} is the specific heat of air,
c_H is the transfer coefficient,
u_a is the wind speed,
T_s is the surface temperature (ice or ocean) and
T_a is the air temperature at the standard level.

Over water, values of c_H as functions of wind speed and atmospheric stability are taken from Smith (1988). Over ice, c_H is constant (Table 2.2).

Latent Heat Upward latent heat flux H_L is given as

$$H_L = -\rho_a L c_E u_a (q_a - q_s) \tag{2.38}$$

where L is the latent heat of vaporization or sublimation,
c_E is the transfer coefficient,
q_a is the specific humidity at the standard level and
q_s is the specific humidity at the surface.

Over ocean, c_E is taken as 1.5 c_H where c_H is from Smith (1988). Over ice, c_E is taken as a constant. The rate of evaporation is determined from (2.38) as H_L/L.

Specific humidity is related to vapour pressure e by

$$q = \frac{\varepsilon e}{p_{atm} - (1-\varepsilon)e} \tag{2.39}$$

where $\varepsilon = 0.622$ is the ratio of molecular weight of water vapour to dry air and p_{atm} is the atmospheric pressure. The specific humidity at the surface is assumed saturated. Saturation vapour pressure over water e_w (in mbar where 1 mbar = 10^2 Pa) at temperature T (°C) from the Smithsonian Meteorological Tables (cited in Gill, 1982) is

$\log_{10} e_w(T) = (0.7859 + 0.03477\ T)/(1 + 0.00412\ T)$.

Saturation vapour pressure over ice e_i (mbar) at temperature T (°C) is

$\log_{10} e_i(T) = \log_{10} e_w(T) + 0.00422\ T$.

Solar Radiation An empirical formulation for incoming short-wave radiation by Shine (1984) is used. The Shine formula for Q_o the short-wave radiation (W m^{-2}) under cloudless skies is

$$Q_o = \frac{S\cos^2 Z}{(\cos Z + 1)e \times 10^{-5} + 1.2\cos Z + 0.0455} \tag{2.40}$$

where S is the solar constant (taken as 1353 W m^{-2}), Z the solar zenith angle and e is the vapour pressure in Pa. The cosine of the zenith angle is

$\cos Z = \sin\phi \sin\delta + \cos\phi \cos\delta \cos HA$

where ϕ, δ and HA are latitude, declination and hour angle respectively. The declination and hour angle are determined by

$\delta = (23.44\ \pi / 180) \cos[(172 - \text{day of year})\ \pi/180)]$

HA = [12 – solar time (h)] $\pi/12$.

The total incoming short-wave radiation is found by modifying Q_o for cloudiness

$$Q = Q_o (1 - 0.6\, C^3) \tag{2.41}$$

where C is the cloud fraction.

Long-wave Radiation Smith and Dobson (1984) give the net long-wave radiation Q_L following Budyko (1974) as

$$Q_L = \varepsilon \sigma\, T_a^3 \left[T_a \left(0.254 - \frac{0.0066}{132.22}\, e \right) (1 - c_1 C) + 4 (T_s - T_a) \right] \tag{2.42}$$

where ε is the emissivity of the surface relative to a black body,
σ is the Stefan Boltzmann constant,
e is the vapour pressure (Pa),
c_1 is a latitude-dependent cloudiness factor,
T_a is the air temperature (K) and
T_s is the surface temperature (K).

Surface Heat Balance

Over open water the net heat flux $H(0)$ is

$$H(0) = H_S + H_L + Q_L . \tag{2.43}$$

The heat flux $H(h)$ conducted through ice of thickness h is

$$H(h) = k_i (T_0 - T_s)/h \tag{2.44}$$

where k_i is the conductivity of ice, T_0 is the temperature at the bottom of ice (assumed the freezing point) and T_s is the surface temperature. The flux (2.44) represents the zero-layer model of Semtner (1976). The heat conducted through the ice balances the net surface flux

$$H_s + H_L - (1 - 0.4\, I_o)\,(1 - \alpha_i)\, Q - Q_L = H(h) \tag{2.45}$$

where α_i is the albedo. A fraction of solar radiation I_o penetrates the ice surface creating brine pockets. In (2.45) we follow Parkinson and Washington (1979) by neglecting 40% of the penetrating radiation and allowing the remaining 60% to heat the surface. I_o is taken as 0.17 (Parkinson and Washington, 1979).

The temperature at the surface of the ice T_s adjusts so that the balance (2.45) is maintained. (2.45) is solved iteratively. If T_s is determined to be above the melting point, then T_s is set to the melting point, the fluxes are recomputed, and the net heat flux melts ice at the upper surface.

Snow has a major effect on albedo, but snow thickness is not modelled in CECOM. α_i in (2.45) is set according to surface temperature following Hibler (1980). The albedo is 0.75 when the surface temperature is below freezing and 0.616 when the surface temperature equals the melting point temperature (Dunlap et al., 2007). The open water albedo is set to 0.1.

Ice, Ocean Fluxes

The heat flux at the ice-ocean interface, F_T, is given by Mellor and Kantha (1989) as

$$F_T = -\rho_o c_p C_{T_z} (T_0 - T) \tag{2.46}$$

where c_p is the specific heat of seawater and T is the temperature at the uppermost model grid point. The transfer coefficient, C_{T_z}, is defined by

$$C_{T_z} = \frac{u_*}{P_{r_t} \kappa^{-1} \ln(-z/z_0) + B_T} \tag{2.47}$$

$$B_T = b\left(\frac{z_0 u_*}{\nu}\right)^{1/2} P_r^{2/3}$$

where $u_* = (\tau/\rho_o)^{1/2}$ is the surface friction velocity,

$P_{r_t} = 0.85$ is the turbulent Prandtl number,

$\kappa = 0.4$ is the von Karman constant,

z is the vertical coordinate corresponding to T,

z_0 is a roughness parameter (see below),

ν is the molecular viscosity and

$P_r = 12.9$ is the molecular Prandtl number.

The factor B_T parameterises a molecular sublayer. The empirical factor b is taken as 3 (see Mellor and Kantha, 1989).

The roughness length z_0 is a weighted sum of under ice and open ocean roughness lengths

$$\ln z_0 = A \ln z_{0i} + (1 - A) \ln z_{0o} \tag{2.48}$$

again following Mellor and Kantha (1989). The underice roughness length z_{0i} is chosen as 0.05 m for ice thickness 3 m, decreasing linearly to zero as ice thickness goes to zero. The open ocean roughness length z_{0o} is Charnock's wave relation (Charnock, 1955)

$$z_{0o} = 0.015\frac{\rho_o u_*^2}{\rho_a g}. \tag{2.49}$$

The salt flux at the ice, ocean surface is given by Mellor and Kantha (1989) analogously to (2.46) as

$$F_S = -C_{S_z}(S_0 - S) \tag{2.50}$$

where S_0 is the salinity at the ice, ocean interface, S is the salinity at the uppermost grid point and

$$C_{S_z} = \frac{u_*}{P_r \kappa^{-1} \ln(-z/z_0) + B_S} \tag{2.51}$$

$$B_S = b\left(\frac{z_o u_*}{\nu}\right)^{1/2} S_c^{2/3}$$

with $S_c = \nu/\alpha_s = 2432$ the Schmidt number for salt diffusion (α_s is the salt diffusivity).

Ice Growth Rate

The heat balance across an infinitesimal control volume about the ice-ocean interface and atmosphere-ocean interface is

$$F_T = AH(h) + (1-A)H(0) - W_0 L_0 \rho_o \tag{2.52}$$

where W_0 is the mass rate of ice growth and L_0 is the latent heat of fusion. (2.52) expresses the balance that the weighted heat flux just above the interface less the heat flux just below the interface gives the latent heat of ice growth. We assume that heat flux below the interface F_T is uniform in a grid cell.

Ice growth or melt results in a surface salt flux, F_S, of

$$F_S = (W_0 - AW_{AI})(S_I - S) + (1-A)S(E-P) \tag{2.53}$$

where S_I is the salinity of ice, and E and P are the evaporation and precipitation rates, respectively. The term W_{AI} is the ice melt at the upper ice surface which is assumed to run off immediately. The ice melt at the upper surface is discussed following (2.45).

There is one further constraint, that is, the temperature at the ice-ocean interface is at the freezing point as a function of salinity

$$T_0 = T_f(S_0). \tag{2.54}$$

The freezing point relationship used here is that given in Gill (1982).

The set of equations (2.46), (2.50), (2.52), (2.53) and (2.54) is solved simultaneously for F_T, F_S, T_0, S_0 and W_0 thereby determining the ice growth rate.

Frazil Ice

The formation of frazil ice in the model follows Mellor and Kantha (1989). A constraint on the ocean temperature is that it must remain greater than or equal to the freezing point. Suppose that after solving the ocean heat and salt balances the temperature and salinity are T_1 and S_1. If T_1 is below the freezing temperature $T_f(S_1)$ then temperature and salinity are changed to a new state T_2 and S_2 with the formation of frazil ice. If the mass fraction of frazil ice is γ, heat and salt balances give

$$T_2 = T_1 + \gamma L_0/c_p \tag{2.55}$$

$$S_2 = S_1 + \gamma(S_1 - S_I).$$

The solution of (2.55) is

$$\gamma = \frac{c_p T_f(S_1) - T_1}{L_0 - c_p\left[T_f(S_1) - T_f(S_I)\right]} \tag{2.56}$$

if the dependence of the freezing point on salinity $T_f(S)$ is linear. The frazil ice is assumed for simplicity to consolidate immediately on the underside of ice. Note that the amount of frazil ice formed is sensitive to the parameterisation of surface heat flux F_T in (2.46). If the parameterisation of F_T is an overestimate, then the under-ice growth will be too small but the frazil ice growth will be too large. Alternatively, if the parameterisation of F_T is an underestimate, then the under-ice growth will be too large but the frazil ice will be too small. The total ice growth is not overly sensitive to the parameterisation (2.46) but depends on atmospheric cooling and heat fluxes within the ocean.

Table 2.2 Constants and parameters for thermodynamics

Symbol	Parameter	Value
c_{pa}	specific heat of air (2.37)	1005 J kg^{-1} K^{-1}
c_H	sensible heat transfer coefficient over ice (2.37)	1.75×10^{-3}
L	latent heat of vaporisation (2.38)	2.5×10^{6} J kg^{-1}
L	latent heat of sublimation (2.38)	2.8×10^{6} J kg^{-1}
c_E	latent heat transfer coefficient over ice (2.38)	2.1×10^{-3}
ε	emissivity (2.42)	0.95
σ	Stefan Boltzmann constant (2.42)	5.67×10^{-8} W m^{-2} K^{-4}
α_w	albedo, water (2.7)	0.1
k_I	ice conductivity (2.44)	2.04 W m^{-1} deg C^{-1}
α_i	albedo, ice (2.45)	0.616
α_s	albedo, snow (2.45)	0.75
c_p	specific heat of seawater (2.46)	3.99×10^{3} J kg^{-1} deg C^{-1}
ν	seawater kinematic viscosity (2.47)	1.8×10^{-6} m^{2} s^{-1}
S_I	salinity of ice (2.53)	5
L_0	latent heat of fusion (2.53)	3.32×10^{5} J kg^{-1}

3 Finite Difference Implementation

3.1 POM

The equations governing the ocean dynamics support the propagation of fast moving external gravity waves and slow moving internal waves. A mode splitting technique is used to separate the vertically-averaged velocity (external mode) from the vertically-varying velocity (internal mode). For the external mode, the depth-integrated continuity equation (A2.2) and depth-integrated momentum equations (A2.3) and (A2.4) use a short time step with terms involving depth-varying velocity fixed. The external model provides sea level elevation η and depth-averaged velocity $\overline{us_k}$, $\overline{vs_k}$ so that internal mode equations can be integrated with a much longer time step.

POM employs a C grid in the horizontal. It is implemented on an orthogonal curvilinear coordinate system which includes Cartesian coordinates and spherical coordinates as special cases. Generalised sigma coordinates are used in the vertical.

For open ocean boundary conditions we use the flow relaxation scheme (FRS) of Martinsen and Engedahl (1987) which has been applied by Slordal et al. (1994). The FRS boundary conditions require a relaxation zone along each open boundary. At the exterior of the FRS zone we specify a solution ϕ_{ext}. For each time step we calculate a solution ϕ_{int} in the interior from the model equations. We then obtain the solution ϕ in the FRS zone by relaxation

$$\phi = \alpha\phi_{\text{ext}} + (1 - \alpha)\phi_{\text{int}}. \qquad (3.1)$$

The relaxation parameter α is 1 at the exterior of the FRS zone and varies smoothly towards 0 at the interior boundary of the zone. Here we choose α as

$$\alpha = 1 - \tanh(2x_E/L_E) \tag{3.2}$$

where L_E is the width of the FRS zone, $x_E = 0$ at the exterior boundary and $x_E = L_E$ at the interior boundary. We choose L_E as five grid intervals.

We apply the FRS boundary conditions to sea level elevation, the horizontal components of velocity, temperature and salinity. We specify values of vertical velocity and turbulence quantities at FRS exterior boundaries but do not relax these quantities.

3.2 Ice Dynamics

The spatial finite difference grid for the ice model defines ice velocity at grid cell vertices and ice concentration at the grid cell centers. The finite difference procedures for solving the momentum balance, the ice stress terms, and the ice advection equation (including the diffusion terms) are described by Hibler (1979). The point relaxation solution for the internal ice stress of Hibler has been replaced by a more efficient line relaxation scheme devised by Zhang and Hibler (1997). A spherical coordinate system is used; the governing equations are given in Zhang and Hibler (1997).

3.3 Mechanical Redistribution of Ice

Thickness Distribution Function

The finite difference thickness distribution discussed in this section and the discrete redistribution function and ridging function discussed in subsequent sections follow Flato (1994). In finite difference form we define M discrete ice categories. In Figure 3.1 we show the thickness categories and the other discrete variables. The thickness boundaries are $h_0, h_1, \ldots, h_M$. In general, the thickness intervals are unequal. The centers of the thickness intervals are given by $h_1^c, h_2^c, \ldots, h_M^c$. h_1^c is defined as 0 and the first thickness category represents open water. The discrete thickness distribution is defined

$$g_i = \int_{h_{i-1}}^{h_i} g(h)dh \qquad i = 1 \ldots M. \tag{3.3}$$

g_i is the fraction of area occupied by the ith thickness category. The cumulative thickness distribution is

$$G_i = \begin{cases} 0 & i = 0 \\ \sum_{j=1}^{i} g_j & i = 1 \ldots M. \end{cases} \tag{3.4}$$

(The subscript notation here differs from Flato, 1994). The ice volume per unit area (mean ice thickness) corresponding to (2.24) is

$$\bar{h} = \sum_{i=1}^{M} h_i^c g_i \ . \tag{3.5}$$

The change in the discrete thickness distribution (corresponding to (2.25)) is

$$\frac{\partial g_i}{\partial t} + \nabla \cdot (\mathbf{u}_{ice} g_i) = F_{i-1} - F_i + \Psi_i + diffusion \ . \tag{3.6}$$

Ψ_i is the discrete mechanical redistribution function (discussed next). F_i is a flux of ice from one category to the next from growth or melt (discussed in Section 3.4).

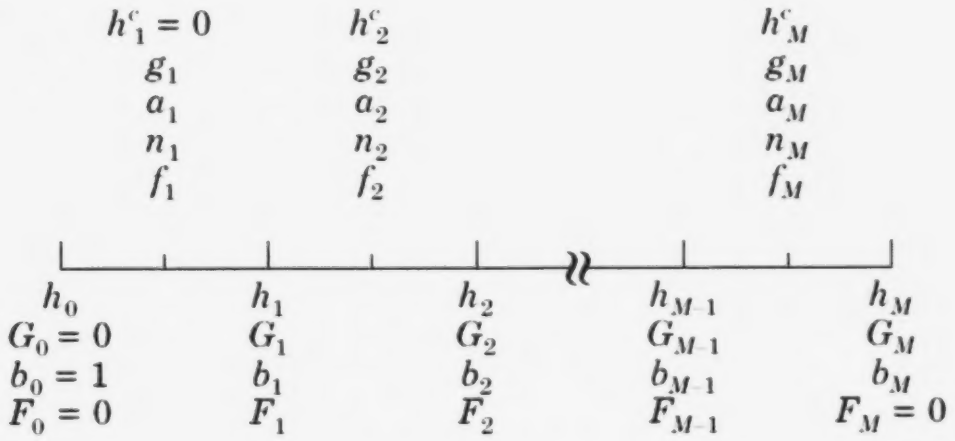

Figure 3.1. Schematic diagram showing the thickness boundaries and locations at which the discrete variables are defined.

Redistribution Function

The discrete redistribution function Ψ_i for Hibler's (1979) plastic rheology is defined from (2.29) as

$$\Psi_i = \begin{cases} \frac{1}{2}\left(\Delta + \dot{\varepsilon}_{jj}\right) + W_{ri}\frac{1}{2}\left(\Delta - \dot{\varepsilon}_{jj}\right) & i = 1 \\ W_{ri}\frac{1}{2}\left(\Delta - \dot{\varepsilon}_{jj}\right) & i = 2 \ldots M \end{cases} \tag{3.7}$$

where W_{ri} is the discrete ridging function.

Ridging Function

The discrete participation function b_i (corresponding to (2.32)) is defined at thickness boundaries

$$b_i = 1 - \frac{G_i}{G^*} \qquad i = 0 \ldots M. \tag{3.8}$$

The discrete distribution function a_i governing the ice which contributes to ridging (corresponding to (2.31)) is

$$a_i = \begin{cases} g_i \dfrac{b_{i-1} + b_i}{2} & b_i \geq 0 \\ g_i \dfrac{b_{i-1}}{2} \dfrac{(h^* - h_{i-1})}{(h_i - h_{i-1})} & b_{i-1} > 0 > b_i \\ 0 & 0 > b_{i-1} \end{cases} \tag{3.9}$$

where h^* is interpolated as

$$h^* = h_{i-1} + \frac{h_i - h_{i-1}}{b_{i-1} - b_i} b_{i-1}. \tag{3.10}$$

a_i is defined for $i = 1 \ldots M$.

The discrete distribution function n_i governing the thickness into which the ridging occurs [corresponding to (2.34)] is

$$n_i = \sum_{j=1}^{M} \gamma_{ji} a_j \qquad i = 1 \ldots M. \tag{3.11}$$

The function γ_{ji} transfers ice from the jth category to the ith category. Before normalisation it can be written

$$\hat{\gamma}_{ji} = \begin{cases} 1/k & h_{i-1} \leq k h_j^c < h_i \\ 0 & \text{otherwise} \end{cases} \qquad j = 1 \ldots M, \quad i = 1 \ldots M - 1.$$

When $i = M$ the criterion for $\hat{\gamma}_{ji}$ to be nonzero is modified to $h_{M-1} \leq k h_j^c$ i.e. ice which would otherwise ridge into a thickness greater than the upper limit is placed into the maximum ice thickness category. The transfer function is normalised to satisfy (2.36)

$$\gamma_{ji} = \hat{\gamma}_{ji} \frac{h_j^c}{\sum_l h_l^c \hat{\gamma}_{jl}} \qquad i, j = 1 \ldots M. \tag{3.13}$$

The discrete ridging function (corresponding to (2.30)) may now be written

$$W_{ri} = \frac{-a_i + n_i}{\sum_{j=1}^{M} (a_j - n_j)} \tag{3.14}$$

and substituted into the redistribution function (3.7).

3.4 Thermodynamic Redistribution of Ice

The implementation of the discrete thermodynamic redistribution described in this section follows Hibler (1980). Heat budgets (2.43) to (2.45) are solved at the water surface and the surface of ice for each ice category and determine the heat flux through ice. The ice growth rates f_i at h_i^c in the ice distribution equation (2.25) are determined from the heat fluxes and the ocean heat balance according to (2.52).

The flux of ice between categories, F_i, in (3.6) is defined from the ice growth rates by an upstream difference

$$F_i = \frac{\max(f_i, 0) g_i + \min(f_{i+1}, 0) g_{i+1}}{h_{i+1}^c - h_i^c}. \tag{3.15}$$

The fluxes must satisfy two constraints. The first is that the flux of ice between categories does not change the total area of ice. The second is that the change in ice volume must equal the ice grown or melted. With M ice categories the rate of change in ice area per unit area expressed in terms of fluxes is

$$\sum_{i=1}^{M} (F_{i-1} - F_i). \tag{3.16}$$

The change is zero provided that $F_0 = F_M = 0$. Considering the second constraint, the rate of change of volume of ice grown or melted per unit area is

$$\sum_{i=1}^{M} f_i g_i \,. \tag{3.17}$$

Expressed in terms of the fluxes, the rate of change in ice volume is

$$\sum_{i=1}^{M}(F_{i-1}-F_i)h_i^c$$

$$=\sum_{i=1}^{M-1}F_i\left(h_{i+1}^c-h_i^c\right)$$

$$=\sum_{i=1}^{M-1}\left[\max(f_i,0)g_i+\min(f_{i+1},0)g_{i+1}\right] \tag{3.18}$$

$$=\max(f_1,0)g_1+\sum_{i=2}^{M-1}f_ig_i+\min(f_M,0)g_M\ .$$

(3.17) and (3.18) are equal except in the case of f_1 negative (open water is absorbing heat) and the case of f_M positive (ice from the thickest category is growing). The fluxes F_i in (3.15) must then be modified to account for these two cases in addition to the requirements following (3.16).

Open Water Absorbing Heat

In the case of open water absorbing heat we specify that the heat is mixed under the ice and contributes to melt at the bottom surface of the ice. We modify the rates of change of ice thickness to f_i'

$$f_i'=\begin{cases}0 & i=1\\ f_i+(1-A)f_1/A & i>1\end{cases} \tag{3.19}$$

where A is the total ice concentration. Note that (3.19) preserves the net rate of ice growth

$$\sum_{i=1}^{M}f_i'g_i=\sum_{i=1}^{M}f_ig_i\ . \tag{3.20}$$

Growth of Thickest Ice Category

The second case in which flux of the form (3.15) does not balance the change in ice volume is when the thickest ice is growing. In this case we add thick ice growth proportionally to all ice categories. Let

$$C_1=\frac{f_Mg_M}{\bar{h}}\ . \tag{3.21}$$

Then define the flux

$$F_{thick,i} = \begin{cases} -C_1 A & i = 1 \\ C_1 g_i & i > 1. \end{cases} \tag{3.22}$$

The flux (3.22) has the property that the increase of ice area is balanced by a decrease in open water area. Note also that the total rate of increase in ice volume from $F_{thick,i}$ balances the rate of increase of volume from growth of the thickest ice category, i.e.

$$\sum_{i=2}^{M} F_{thick,i} h_i^c = f_M g_M . \tag{3.23}$$

Maximum Rate of Decay

Hibler (1980) suggests applying a maximum rate of ice decay (minimum growth rate) f_{min} taken here as –0.15 m day^{-1}. We modify the ice growth rates

$$f_i'' = \max(f_{min}, f_i') g_i . \tag{3.24}$$

The difference between f_i'' and f_i' represents excess heat which melts ice laterally. The excess rate of decay is

$$Excess = \sum_{i=1}^{M} (f_i'' - f_i') g_i . \tag{3.25}$$

Similarly to the thick ice growth we allocate this decay proportionately to all ice categories. Define

$$C_2 = \frac{Excess}{\bar{h}} \tag{3.26}$$

then the lateral melt in terms of a flux is

$$F_{lateral,i} = \begin{cases} C_2 A & i = 1 \\ -C_2 g_i & i > 1. \end{cases} \tag{3.27}$$

The redistribution of ice from growth or melt can be finally written as

$$\frac{\Delta g_i}{\Delta t} = F_{i-1} - F_i + F_{lateral,i} + F_{thick,i} . \tag{3.28}$$

4. Canadian East Coast Ocean Model (CECOM)

The region of interest for the model extends from the Gulf of Maine in the south to Baffin Bay in the north. The model is implemented on a spherical coordinate system. To reduce the impact of converging meridians, we select a spherical coordinate system that is rotated relative to the earth's longitude and latitude so that the equator of the rotated system bisects the domain. In the following sub-sections, the coordinate transformation and model domain are described.

4.1 Rotated Spherical Coordinates

The relation between Cartesian coordinates (x, y, z) and longitude and colatitude (ϕ, θ) (refer to Figure 4.1) is

$$\begin{aligned} x &= \sin\theta\cos\phi \\ y &= \sin\theta\sin\phi \\ z &= \cos\theta \end{aligned} \tag{4.1}$$

where we take the radius of the sphere as unity. Consider the transformation from original coordinates $\mathbf{r}$ to coordinates in a rotated system $\mathbf{r}'$

$$\mathbf{r} = \begin{pmatrix} x \\ y \\ z \end{pmatrix} \Rightarrow \mathbf{r}' = \begin{pmatrix} x' \\ y' \\ z' \end{pmatrix}. \tag{4.2}$$

A rotated system can be defined by the successive application of three rotations (Figure 4.2):

1. angle ξ about the z axis,
2. angle η about the new y axis and
3. angle ζ about the new z axis.

The angle of rotation is in the clockwise direction looking in the direction of the axis. The transformations from $\mathbf{r}$ to $\mathbf{r}'$ and components of vectors are given in Appendix 2.

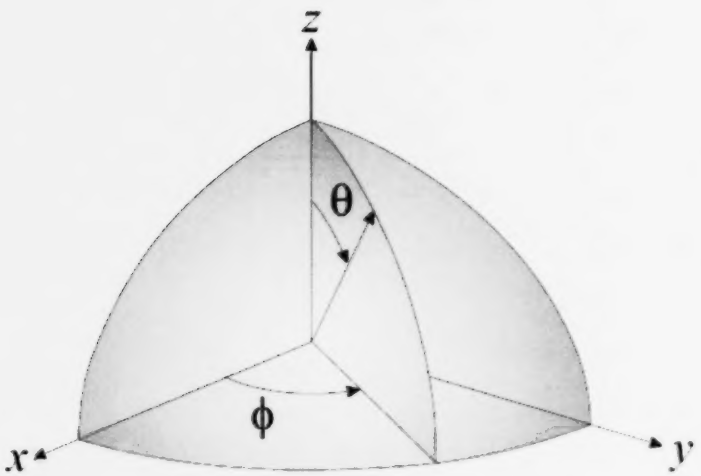

Figure 4.1 Spherical coordinate system with longitude ϕ and co-latitude θ.

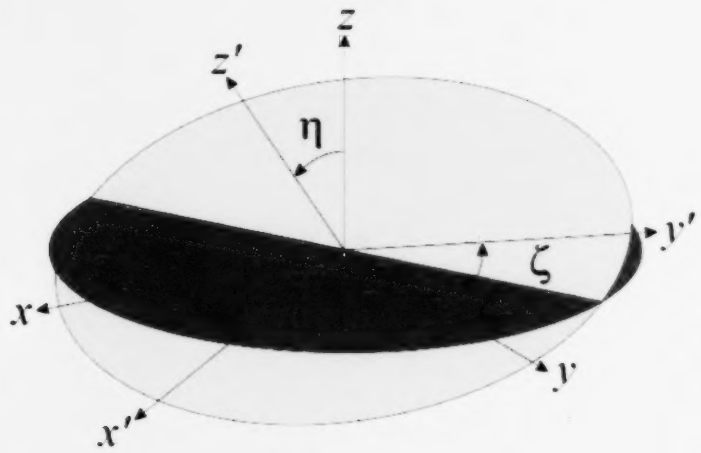

Figure 4.2. The decomposition of a coordinate system rotation into three successive rotations of ξ, η and ζ. The red line is the y axis after one rotation.

4.2 The CECOM Domain

The CECOM model grid has a resolution of 0.1° × 0.1°. As noted, it is defined on a rotated, spherical coordinate system (Figure 4.3). The model domain in the geography

coordinates, and the inner and outer boundaries are shown in Figure 4.4. The bathymetry of the domain is drawn in Figure 4.5. Specifics of the domain are given in Table 4.1.

Generalised sigma coordinates are used to retain near-surface resolution even as bottom depth increases. The procedure we use to select the vertical levels is somewhat arbitrary. For sufficiently deep water (bottom depth greater than or equal to H_1) we specify that a fixed upper layer and the underlying ocean each have a given number of levels. The levels are scaled according to the fixed upper or varying lower layer thickness. For shallow water (bottom depth less than or equal to H_0) all levels are distributed uniformly. Between H_0 and H_1 the levels are linearly interpolated between the levels for H_0 and H_1.

H_0 = 10 m, H_1 = 64 m and an upper layer thickness of 64 m are selected. There are a total of 21 levels, with 8 levels in the upper layer and 13 levels in the underlying ocean (at depths greater than H_1). These generalised coordinates are shown for a section across the Labrador shelf (27° longitude in rotated coordinates) in Figure 4.6.

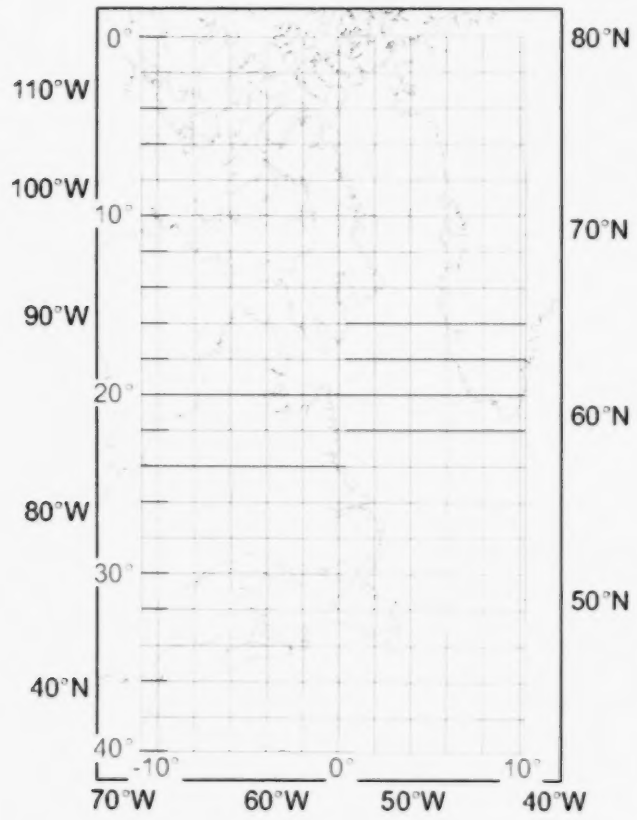

Figure 4.3. CECOM grid defined by a rotated spherical coordinate system. Lines of longitude and latitude in the rotated system are drawn in red.

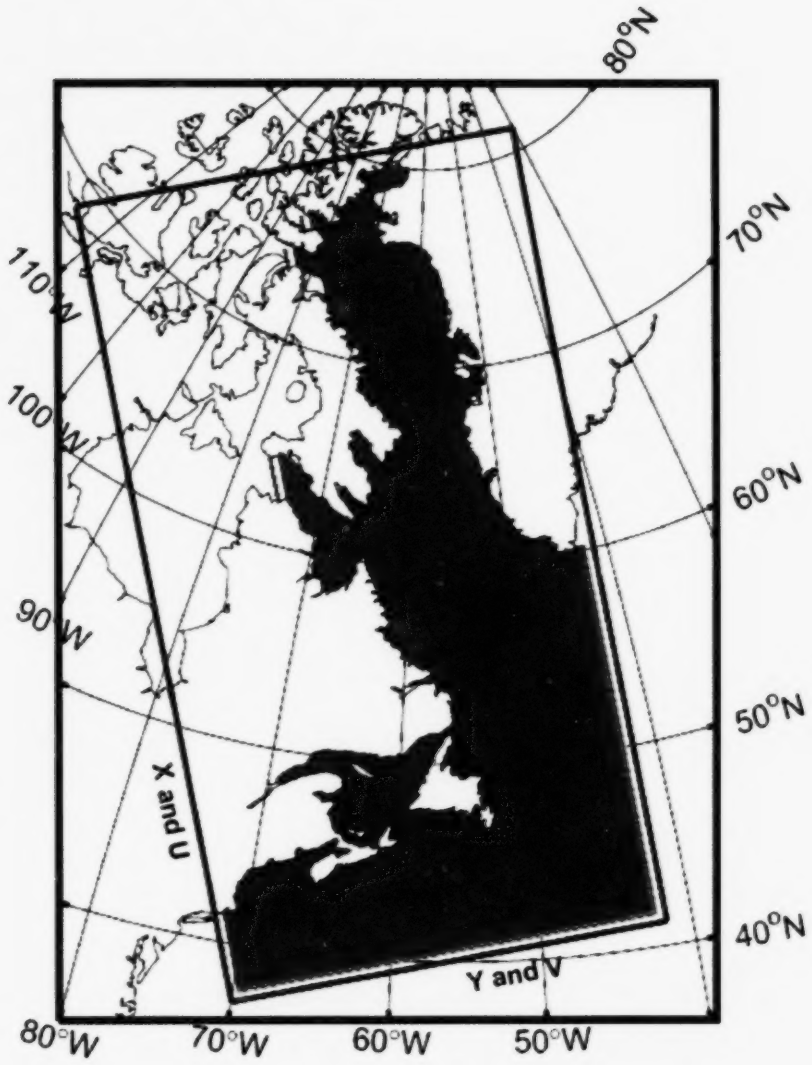

Figure 4.4. CECOM domain (green) in the geographic coordinates. The double red lines are the inner and outer boundaries of the model. The blue box is the boundary in the rotated system of Fig. 4.3.

Table 4.1 Specifications of the CECOM domain

Coordinate rotation	$(\xi, \eta, \varsigma) = (41°, 82°, -171°)$
Extent (rotated coordinates)	0 to 40° longitude, −11 to 10.3° latitude
Horizontal resolution	0.1° × 0.1°
Dimension	400 × 213 × 21 (east × north × vertical)
	410 × 223 × 21 including boundary relaxation zones
time step	450 s (internal)
	15 s (external)

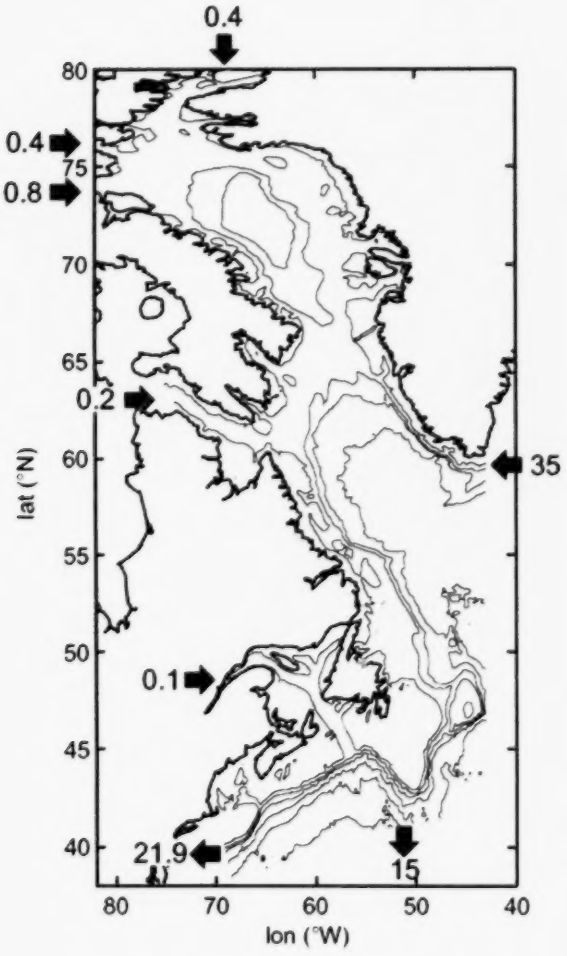

Figure 4.5. The bathymetry of the CECOM domain. Depth contours of 200, 1000, 2000, ... m are drawn. Specified transports (Sv) at open ocean boundary are indicated.

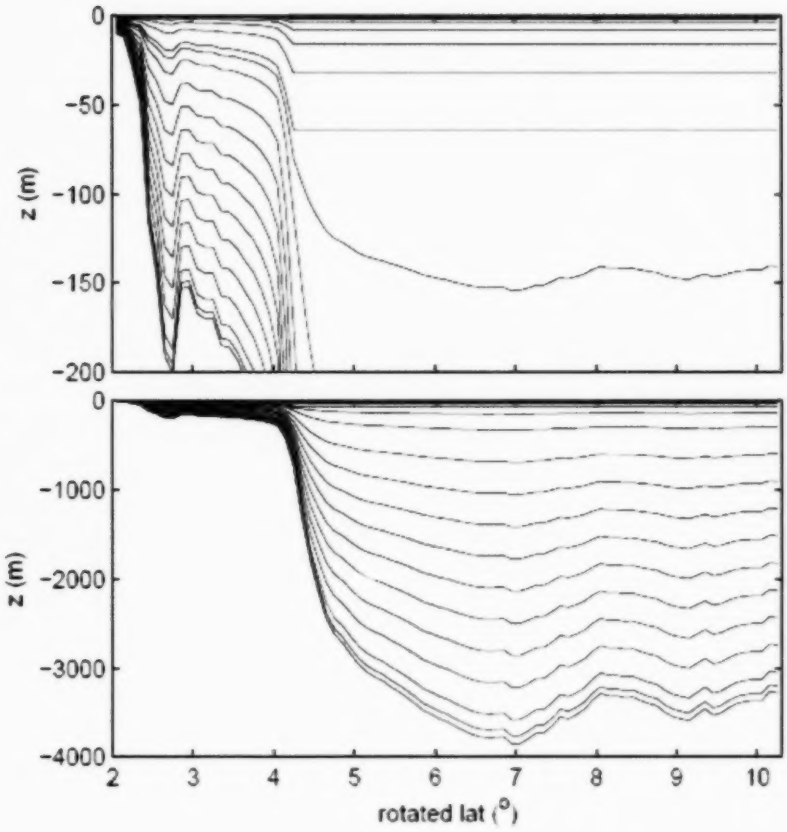

Figure 4.6. A cross-section of the generalized coordinates across the Labrador Shelf. The upper panel shows the coordinates over the upper 200 m.

4.3 Ocean Initial State, Boundary Conditions and Model Spin-up

Monthly, climatological ocean temperature and salinity are used as an initial state and as open ocean boundary conditions. The monthly climatologies were obtained from an objective analysis of historical data archived at Bedford Institute of Oceanography (Tang, 2007). The database covers an area from northern Baffin Bay to Cape Hatteras and from the coast to 42° W. It is derived from a variety of sources dating back to 1910. The objective analysis employed an iterative difference correction procedure with topography-dependent radii of influence. The grid resolution is 1/6° × 1/6°. Figure 4.7 is a sample plot from the data set showing surface temperature and salinity for September.

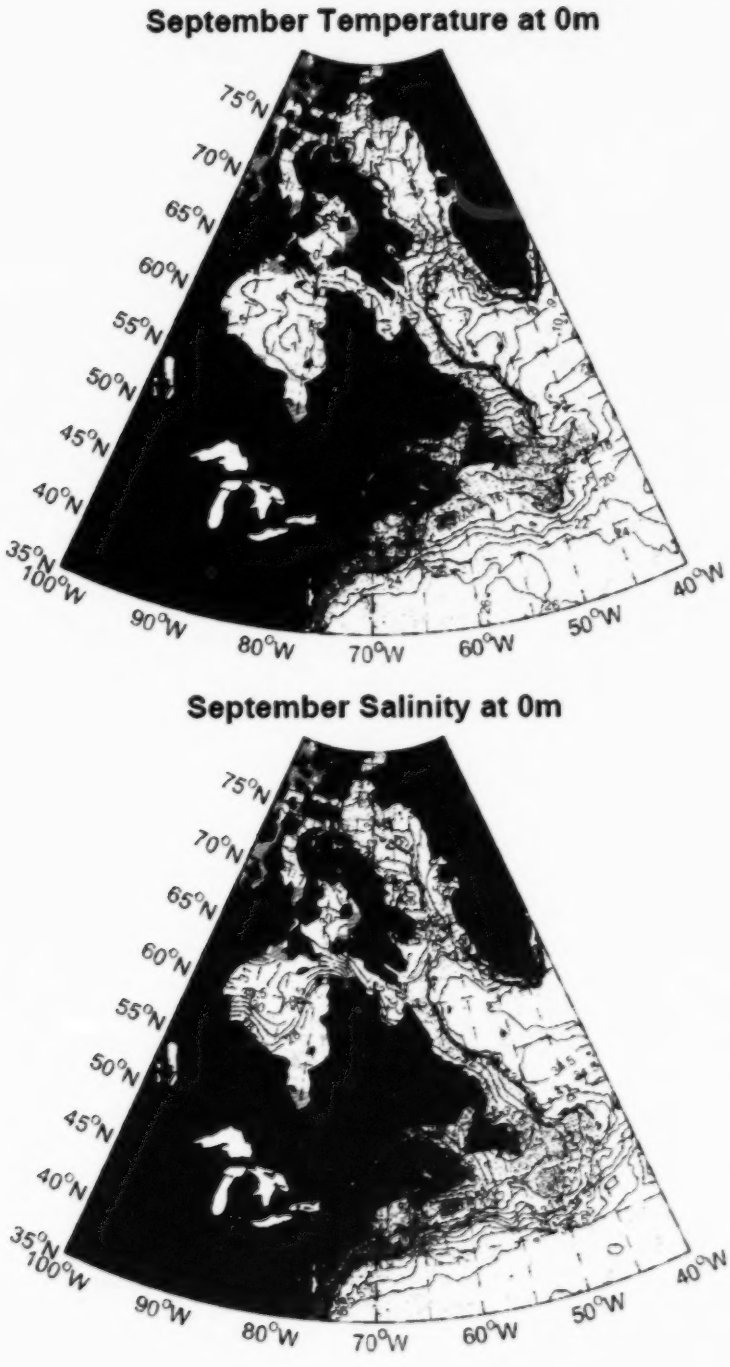

Figure 4.7. Surface temperature and salinity for September from objective analysis. The red dots are the locations of the raw data.

Transports based on large-scale models and observations are specified at the open boundaries of the model (Clarke,1983; Ezer and Mellor, 1994). In the present implementation, the transports as shown in Figure 4.5 are used. Different specifications are being tested to obtain best results. The vertical profile of normal velocity is determined by the density through the geostrophic relation. The sea level elevation at the open boundaries is determined by geostrophy to within a constant.

The model open ocean boundary (double red lines in Fig. 4.4) is interrupted by land masses. The procedure to determine sea level in the ocean straits (Nares Strait, Lancaster Sound, Jones Sound, Hudson Strait and St. Lawrence Estuary) is as follows. We spin up the model with three diagnostic runs of 10 days duration, each with zero wind stress. The sea level at open boundaries of straits is set to the adjacent interior value from the end of the previous run. The spin-up concludes with a 10-day prognostic run.

The initial state consists of September temperature and salinity and zero ice. We create 12 open ocean boundary conditions corresponding to the monthly temperature and salinity fields. As noted previously, the geostrophic relation determines sea level elevation only to within a constant. The constants, i.e. the sea level average across open boundaries in straits, are determined from the spin-up. The monthly boundary conditions are linearly interpolated to daily values. The sea level elevation and transport stream function after the spin-up process are drawn in Figure 4.8.

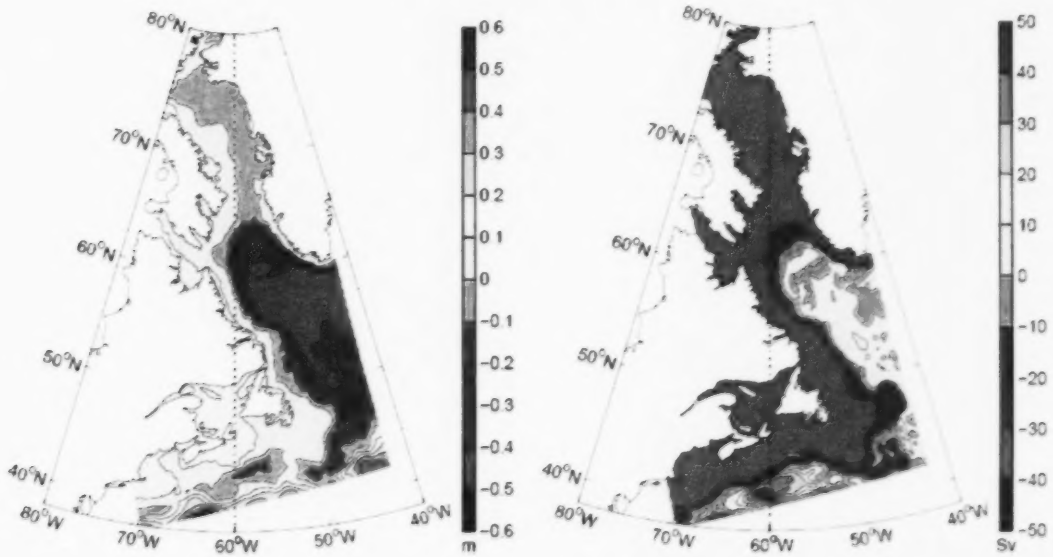

Figure 4.8. The sea level elevation (left) and transport stream function (right) following the spin-up process.

4.4 Ice categories

The ice model is implemented with 10 ice thickness categories with boundaries at 0.05, 0.18, 0.38, 0.66, 1.06, 1.58, 2.24, 3.04, 3.98 and 5.04 m. The corresponding central thicknesses, h_i^c, are 0, 0.12, 0.28, 0.52, 0.86, 1.32, 1.91, 2.54, 3.51 and 4.51 m.

5. Model Physics of WaveWatch III (WW3)

The WAVEWATCH III (hereafter WW3) wave model (version 2.22) is used in the BIO forecasting system to forecast wave height and direction. This is a WAM-type ocean surface wave model developed at NOAA/NCEP (Tolman and Chalikov,1996; Tolman, 2002). It has been successfully applied in global and regional scale studies in many areas including the North Atlantic, and has proven to be an effective tool to study wave spectral evaluation, air-sea interactions and nonlinear wave-wave interactions. WW3 is a discrete spectra and phase-averaged model (Battjes 1994).

For regional and global applications, the directional wave spectrum is resolved at each model grid point in terms of wavenumber-direction bands and the evolution of the wave field is found by numerically solving the spectral wave action balance equation, which is usually written as

$$\frac{\partial N}{\partial t}+\frac{1}{\cos\phi}\frac{\partial}{\partial\phi}\dot{\phi}N\cos\theta+\frac{\partial}{\partial\lambda}\dot{\lambda}N+\frac{\partial}{\partial k}\dot{k}N+\frac{\partial}{\partial\theta}\dot{\theta}_g N=\frac{S}{\sigma}\ . \qquad (5\text{-}1)$$

where λ is longitude, ϕ is latitude, θ is wave propagation direction, k is wave number, t is time, σ is the intrinsic angular frequency. WW3 evaluates the balance equation for the wave action spectrum $N(k,\theta,x,t)$ which is usually expressed in spherical coordinates (Komen et al., 1994).

The derivatives in (5-1) are the propagation velocities in physical and spectral domains $\dot{\phi}=\frac{c_g\cos\theta+U_\phi}{R}$, $\dot{\lambda}=\frac{c_g\sin\theta+U_\lambda}{R\cos\phi}$, $\dot{\theta}_g=\dot{\theta}-\frac{c_g\tan\phi\cos\theta}{R}$, R is the radius of the earth, and U_ϕ and U_λ are current components in ϕ and λ directions. The left side of equation (1) represents the local rate of change of wave action density, propagation in physical space, action density shifting in frequency and direction due to the spatial and temporal variation in depth and current. The net source term S consists of wind input(S_{in}),white-capping dissipation(S_{ds}), nonlinear wave-wave interactions(S_{nl}), and bottom friction(S_{bot}). WW3 uses an explicit scheme to solve the action balance equation (1) for N.

Two combinations of the source terms S_{in} and S_{ds} are available in WW3. The default set up of WW3 corresponds to the wave-boundary layer formulation for S_{in} and S_{ds}, due to Tolman and Chalikov (1996). Tolman (2002) notes that application of this formulation has entailed a

correction in fetch-limited wave heights that results from atmospheric stratification, which necessitates a re-tuning of the model by defining an 'effective' wind, as well as an additional correction for the impact of stability on wave growth. An alternate combination corresponds to WAM cycle 3 physics (hereafter denoted WAMC3 physics), in which S_{in} and S_{ds} are based on WAMDI (1988), Snyder *et al.* (1981) and Komen *et al.* (1994). Quadruplet nonlinear interactions S_{nl} are simulated by DIA, and bottom dissipation S_{bf} , by the JONSWAP parameterization of Hasselmann *et al.* (1973). *Padilla-Hernãndez* et *al.* [2007] compared the WW3 model against WAM and SWAN models for two North Atlantic storms and found that WW3 provided the high quality statistical comparisons to deep water observations.

6. The Bedford Institute Ocean Forecasting System (BIOFS)

BIOFS is a real-time short-term (2-day) forecasting system for eastern Canadian waters. The forecast period is constrained by input data from Environment Canada. If meteorological data from long range weather forecasts are available, the ocean forecasts can be extended to a longer period. It consists of two sub-systems: one for CECOM (Section 6.3) and one for WW3 (Section 6.4). Graphic display of the forecasts can be viewed at the following public website maintained by DFO:

http://www.mar.dfo-mpo.gc.ca/science/ocean/icemodel/ice_ocean_forecast.html

The parameters displayed on the website are surface trajectories, water level time series at selected locations, ice concentration and thickness, wave height and direction (Northwest Atlantic and Atlantic Maritimes), sea surface elevation (non-tidal) maps, temperature at surface and 50 m. They are given at hourly (water level time series), 6-hourly (wave) or 12-hourly (all others) intervals.

6.1 Input Data

Meteorological Data

Meteorological forcing is taken from the Canadian Meteorological Centre (CMC) Global Environmental Multiscale (GEM) model (Mailhot *et al.*, 2006), which provides 48 hour forecasts twice daily at 0000 and 1200 UTC, with fields output at 3 hour intervals. The GEM model is an operational atmospheric model that is part of the Canadian Regional Forecast System (RFS) developed by Environment Canada. The model uses a variable resolution grid over the entire globe, with a mesoscale 15 km horizontal resolution window over Northern America. Fields used in the forecasting system are 10m winds, 2m air and dew point temperatures, total cloud coverage, and total accumulated precipitation. All meteorological parameters are linearly interpolated to the ocean and wave model grids. Except for the10 m winds, the parameter values change every 3 hours. For CECOM, the 10m wind field is interpolated in time to the model time step of 7.5 minutes to avoid temporal discontinuities in the dynamical forcing. Total accumulated

precipitation is converted to a precipitation rate. For WW3, the wind fields are interpolated to the propagation time step of the respective wave model (see Section 6.4 for details).

Sea-Ice Data

Ice concentration data are used for data assimilation (Section 6.2) in the ice model and to define the wave domain in WW3. In WW3, a grid point is considered open ocean if the ice concentration is equal or less than 0.5. Otherwise, it is considered land. Digital sea ice charts which include ice concentration data are provided by Canadian Ice Services(CIS). Canadian waters are covered by five digital ice charts (Figure 6.1). Data from Eastern Arctic, Hudson Bay and East Coast are used in the forecasting system. CIS produces daily charts for the Gulf of St.Lawrence and the Labrador and Newfoundland coasts south of 58N. Regional charts for Hudson Bay, Baffin Bay and the Labrador coast north of 58N are produced fortnightly. Typically the regional charts are released several days after the date for which they are valid. Since these charts represent more of a two week average condition than an instantaneous one, BIOFS uses a regional chart's release date as its valid date.

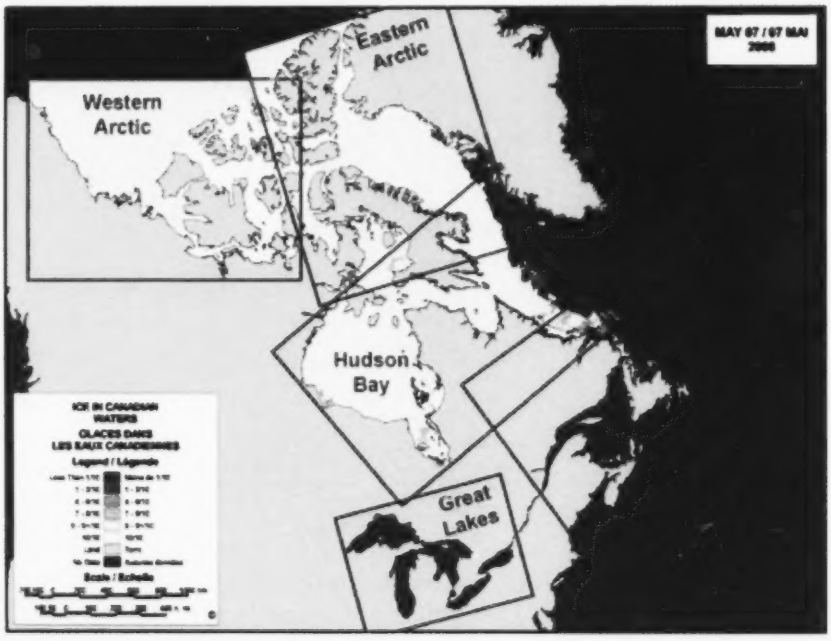

Figure 6.1. Coverage of CIS's digital ice charts (courtesy of CIS).

The digital charts use the "egg code" (Environment Canada, 2005) to indicate the sea ice partial concentration for each stage of development, on a regularly spaced grid. Each "egg" indicates up to three different ice types (ignoring trace amounts), each of which is assigned a stage and concentration. The stage of development may be interpreted as an approximate

measure of the ice thickness. The conversion of stage to ice model thickness category is illustrated in Table 6.1. There are also four special cases listed in Table 6.2.

Table 6.1 Conversion from ice stage to ice model category

Ice stage of development	Description	Ice model category	Ice thickness boundaries (m)
OW, BW, IF	Open Water, bergy water, ice-free	1	$-0.05 < h \leq 0.05$
1	New	2	$0.05 < h \leq 0.18$
2	Nilas	2	$0.05 < h \leq 0.18$
3	Young, Unknown	3	$0.18 < h \leq 0.38$
4	Young, Grey	2	$0.05 < h \leq 0.18$
5	Young, Grey-White	3	$0.18 < h \leq 0.38$
6	First Year, Unknown	4	$0.38 < h \leq 0.66$
7	First Year, Thin	5	$0.66 < h \leq 1.06$
8	First Year, Thin First Stage	5	$0.66 < h \leq 1.06$
9	First Year, Thin Second Stage	5	$0.66 < h \leq 1.06$
1.	First Year, Medium	6	$1.06 < h \leq 1.58$
4.	First Year, Thick	7	$1.58 < h \leq 2.24$
7.	Old	8	$2.24 < h \leq 3.04$
8.	Old, Second Year	9	$3.04 < h \leq 3.98$
9.	Old, Multi-Year	9	$3.04 < h \leq 3.98$
L	Ice of Land Origin	9	$3.04 < h \leq 3.98$
B	Brash	3	$0.18 < h \leq 0.38$

Each stage of development is first converted to a category. The partial concentrations and categories, including flags (Table 6.2), are then nearest-neighbour interpolated to the model grid. Grid points with land fast ice will be filled with neighbouring concentrations and categories. Including flags in the interpolation preserves grid points which should not be filled by interpolation. All the charts available for a forecast date are then combined. Where charts overlap the concentrations of each category are averaged. Flagged points are ignored in the averaging.

Table 6.2 Interpolation of ice data

Ice stage of development	Description	Action
POINT NOT COVERED BY POLYGON	Point is outside CIS analysis area	Flag
LAND	Land point	Flag
ICEGLACE	Useless CIS category indicating ice presence but not providing concentration or stage	Flag
FASTICE	Land fast ice	Nearest Neighbour

Tides

Tidal constituents of elevation and velocity come from two sources. Paturi *et al* (2008) provides eight constituents (M2, S2, N2, K2, K1, O1, P1, Q1) and covers most of the model domain up to Davis Strait. Dunphy *et al* (2005) provides five tidal constituents (M2, S2, N2, K1, O1) for Baffin Bay. Constituents are linearly interpolated to the model grid. Where the two sources slightly overlap at Davis Strait, matching constituents are averaged.

6.2 Data assimilation in CECOM

Many assimilation schemes have been developed for oceanographic and meteorological applications in the past 20 years. Advanced schemes such as 3-d and 4-d variational method and Karmen filter require massive resources and abundant data to yield optimum results. In this section, we describe three methods to assimilate the annual cycle of the temperature and salinity fields, sea surface temperature and ice concentration data into the ocean forecast model.

Assimilation of the Annual Cycle of the Temperature and Salinity Fields

Monthly temperature and salinity climatologies are prescribed at the open boundaries of CECOM. Such constraints are not strong enough to prevent the temperature and salinity fields from drifting in multi-year integration. To ensure the annual cycles are preserved, a nudging term with a constant relaxation time scale, t_R, of 45 days are added to the temperature and salinity equation:

$$\frac{\partial T}{\partial t} = ... + \frac{1}{t_R}(T_{CLIM} - T)$$

$$\frac{\partial S}{\partial t} = ... + \frac{1}{t_R}(S_{CLIM} - S)$$

where T_{CLIM} and S_{CLIM} are monthly temperature and salinity climatologies linearly interpolated to daily intervals.

Assimilation of Sea Surface Temperature Data

Daily near real-time sea surface temperature (SST) derived mainly from satellite observations are provided by CMC. The data are assimilated into the ocean forecast model using a flux correction method. The method is based on the theory of optimal interpolation. A correction term proportional to the differences between the modeled and observed SST is added to the heat flux equation.

We first consider the equation for SST assimilation (see Appendix 4):

$$T^a(t) = T^m(t) + \frac{\varepsilon_m^2}{\varepsilon_m^2 + \varepsilon_o^2} \exp\left[-\frac{(t-t_o)^2}{2\tau^2}\right]\left[T^o(t_o) - T^m(t_o)\right] \qquad (6.1)$$

where the superscripts and subscripts "*a*", "*m*" and "*o*" in (6.1) denote "assimilation", "model" and "observation", respectively. t_o is the time of the most recent observation and t is the model time. ε_m^2 and ε_o^2 are the model and data errors, respectively. τ is the correlation time scale of SST. Since change in SST, ΔT, is related to change in heat flux, ΔQ, by

$$\Delta T = \frac{t_d}{\rho\, c_p h}\, \Delta Q$$

where h is the mixed layer depth and t_d is the time interval of SST data, the first terms on each side of (6.1) can be replaced by the corresponding heat fluxes. The equation for SST data assimilation is:

$$Q^a(t) = Q^m(t) + \frac{\rho c_p h}{t_d} F \exp\left[-\frac{(t-t_o)^2}{2\tau^2}\right]\left[T^o(t_o) - T^m(t_o)\right] \qquad (6.2)$$

where $F = 1/[1 + (\varepsilon_o/\varepsilon_m)^2]$. F ranges from 0 to 1. Not all parameters in (6.2) are well known. To implement (6.2) in the forecast model, the parameters are adjusted to yield optimal results.

Figures 6.2 and 6.3 show the impact of data assimilation on model SST from a test run. In this run, $F = 1$, $t_d = 1$ day, $\tau = 1$ day were used and $h = 20$ m. To reduce model noise in the run, $T^m(t_o)$ in (6.2) was replaced by the model SST averaged over the previous day (from t_0 - 1 day to t_0). Significant improvements in the model SST can be achieved by using this assimilation scheme. Without data assimilation, the difference between the model and data at the Scotian Shelf is of the order of $\sim 2^\circ$C. The difference is reduced to a fraction of a degree with data assimilation. Over the model domain, the model without data assimilation over predicts SST in the northern Labrador Sea and under predicts SST in the coastal and the North Atlantic Current regions (Figs. 6.3). Data assimilation is able to reduce the errors to less than 1°C.

The SST assimilation is applied to ice free waters only. In ice covered areas, the sea surface temperature is equal or very close to the freezing temperature.

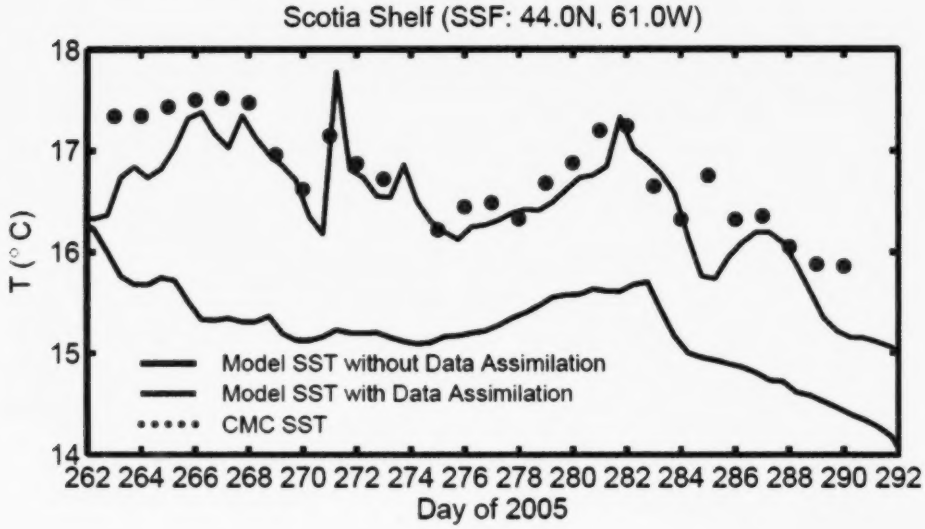

Figure 6.2 A comparison of SST in a 1° x 1° area centered at the indicated location with and without data assimilation.

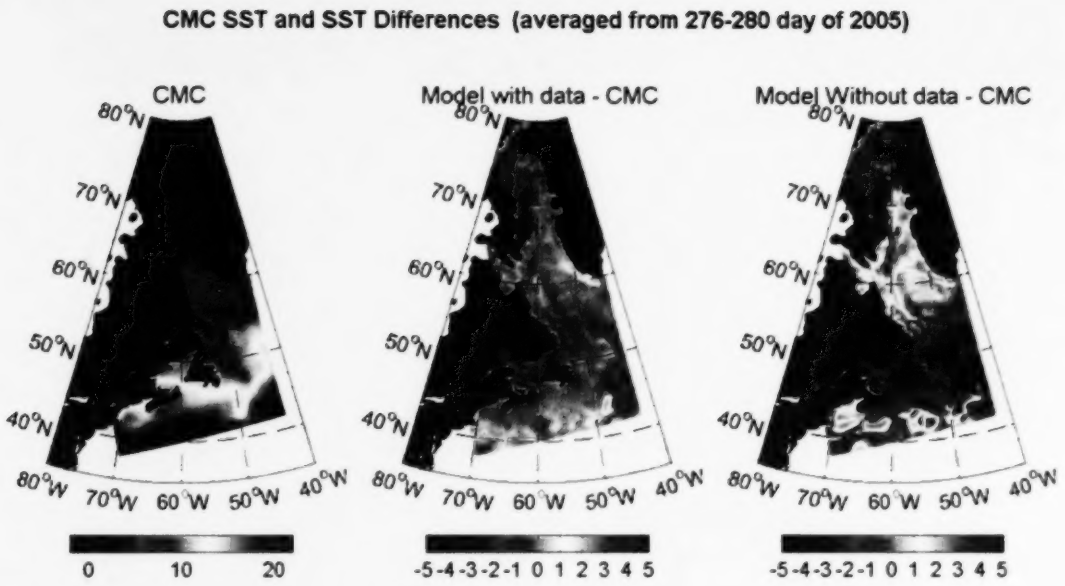
CMC SST and SST Differences (averaged from 276-280 day of 2005)
CMC
Model with data - CMC
Model Without data - CMC
80°N
70°N
60°N
50°N
40°N
80°W 70°W 60°W 50°W 40°W
0 10 20
-5 -4 -3 -2 -1 0 1 2 3 4 5
-5 -4 -3 -2 -1 0 1 2 3 4 5

Figure 6.3 CMC SST (left) and the difference between the model and data with (middle) and without (right) data assimilation.

Assimilation of sea-ice data

An insertion-nudging method is used for ice data assimilation. Ice concentration data are inserted to the model gradually and the model concentration is restored to the data value with a prescribed time constant. In the equation for the thickness distribution function, a term proportional to the difference between the observed and values is introduced:

$$\frac{\partial g_i}{\partial t} + \nabla \cdot (\mathbf{u}_{ice} g_i) + \frac{\partial (f g_i)}{\partial h} = \Psi + diffusion + \Gamma(g_{oi} - g_i) \tag{6.2}$$

where g_{oi} is the ice chart concentrations and g_i is the model concentrations for ice of thickness category *i*. Γ has the following form:

$$\Gamma = \gamma_m \exp\left[-\frac{(t - t_o)^2}{2\gamma_w^2} \right] \tag{6.3}$$

where t is the model time, t_o is the time for which the ice chart is valid. γ_m and γ_w are adjustable parameters. The Gaussian function in (6.3) limits nudging to the times around the ice chart time. $1/\gamma_m$ is the restoring time scale. In the present implementation, the values of $1/\gamma_m$ and γ_w are set to 1.6 hours (5760 seconds) and 3 hours (10800 seconds) respectively. At one hour from the ice chart time this scheme gives a concentration change rate of ~0.5 per hour. At times $\pm 2\gamma_w$ from

the ice chart time the rate is negligible. Where there is no ice chart data, the nudging is not applied.

Figure 6.4 is a comparison of ice area south of 58° with and without data assimilation for January 2008. Figure 6.5 shows the ice concentration from CIS's East Coast ice chart, and the model results with and without data assimilation. The data assimilation significantly reduces the model error. In particular, ice cover in the Gulf of St. Lawrence and the location of the eastern ice edge can be simulated more realistically with data assimilation.

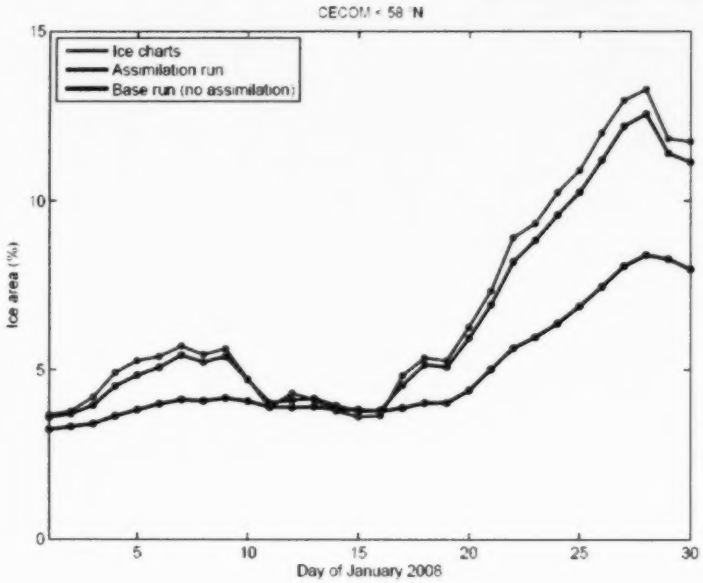

Figure 6.4 A comparison of the model ice area south of 58° N with (blue) and without (black) data assimilation. The unit is percentage of the model area south of 58° N.

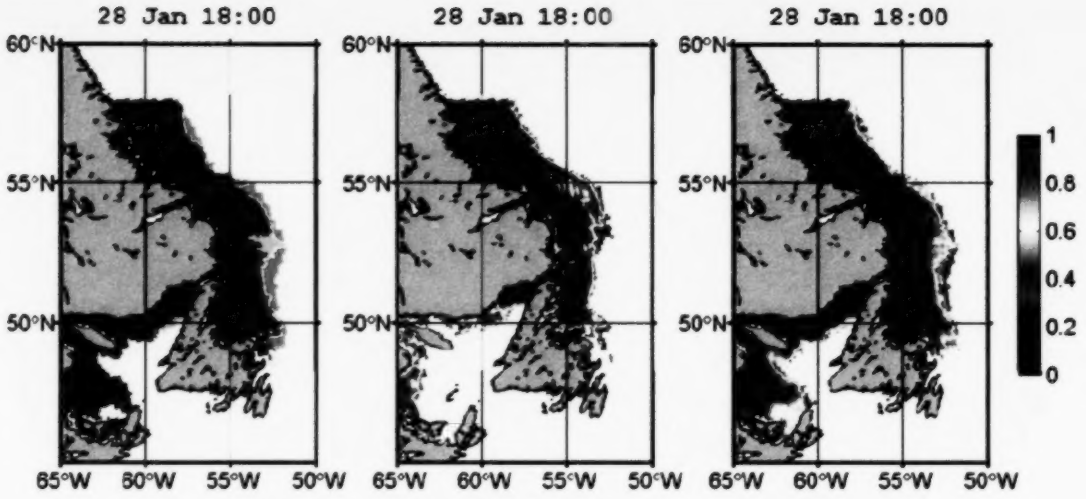

Figure 6.5 Ice concentration for January 28, 2008: data (left), model results without (middle) and with (right) data assimilation.

6.3 Operational Implementation of CECOM

The ice-ocean component of BIOFS is mostly comprised of MATLAB scripts that handle the pre-processing of model input fields, the execution of the CECOM FORTRAN executable, the post-processing of model results, and the management of data files. MATLAB was chosen for its platform independence, interpolation and graphics functionalities, and the abundance of open source tools such as M_Map (Pawlowicz, 2006), readgrib (Blanton, 2005), snctools (Evans, 2007) and T_Tide (Pawlowicz et al, 2002). Scheduling and automation is handled by the Linux bash shell, but could easily be implemented for other platforms and operating systems.

Delivery of Meteorological and ice Data

As with any endeavor in real-time forecasting, the primary concern is the timely delivery of the data required to force the forecast model. To address this concern a separate subsystem, written in bash shell scripts, automates the retrieval of crucial meteorological forecast data transmitted from CMC to BIO server Emerald2 twice a day. The subsystem polls the site for data and performs file checks after retrieval to verify file integrity. There is usually a 5-6 hour delay between the CMC regional forecast and the appearance of the forecast data on their ftp site. If the system fails to retrieve the data, it retries for a predefined number of times.

The digital ice charts, valid for 1800 UTC are delivered daily to an ftp server at BIO, Starfish, at ~2200 UTC. The CIS delivery system itself checks for file integrity after delivery.

Forecast Schedule

CECOM is run three times daily within BIOFS, producing 48 hour forecasts for 0000 and 1200 UTC (Table 6.3, Fig. 6.6). Due to delays in receiving the meteorological data, the CMC 1200 UTC data are received at ~1700-1800 UTC and the forecast completes at ~1800-1900 UTC. A 1200 UTC data assimilation run using 1800 UTC sea ice concentration data and 1200 UTC sea surface temperature data (the same SST are received in the CMC 0000 UTC forecast data) is made the following morning at ~0300 UTC to assimilate the most recent ice chart and sea surface temperature data. The 0000 UTC forecast is run four hours following the data assimilation run at ~0700 UTC.

Table 6.3 Ocean forecast schedule. Both the local time "AT" (Atlantic Time) and UTC are indicated.

Day 1			**Day 2**		
1 – 2 pm AT	2 – 3 pm AT	6 pm AT	11 pm AT	1 – 2 am AT	3 am AT
1700-1800 UTC	1800-1900 UTC	2200 UTC	0300 UTC	0500-0600 UTC	0700 UTC
CMC 1200 UTC forecast data received	1200 UTC 48-hour forecast	CIS charts received	1200 UTC 48-hour ice and SST assimilation	CMC 0000 UTC forecast data received	0000 UTC 48-hour forecast

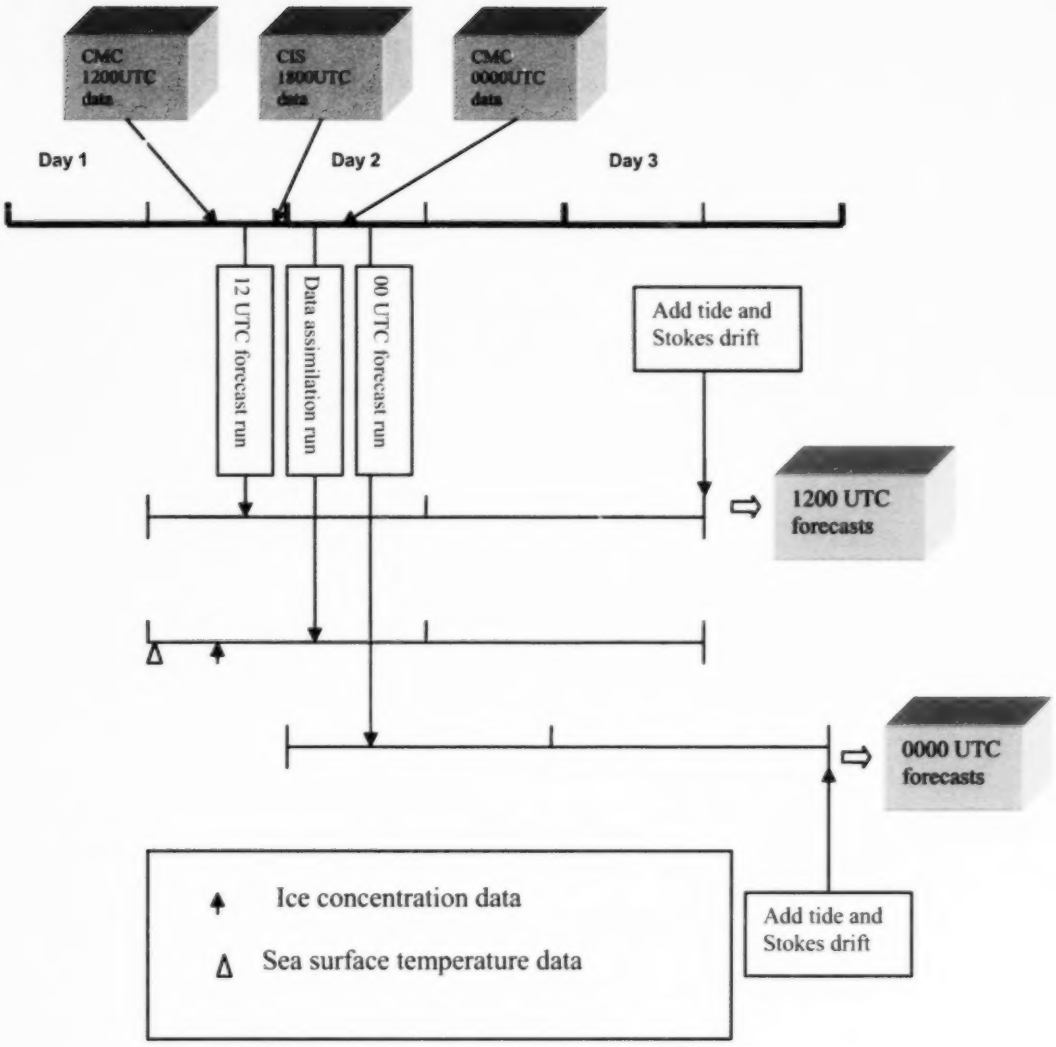

Figure 6.6 Flow chart of the forecasting operations in a 24-hour period.

Forecast Methodology

Each forecast is initialized with the most recent output of a previous forecast. The ocean lateral boundary conditions are linearly interpolated to daily values from the monthly means to prevent discontinuity. The boundary conditions also provide a constraint for temperature and salinity near the boundaries. In the interior, nudging and statistical interpolation are used to prevent long-term drifts and to assimilate sea surface temperature data into the model (see Section 6.2).

After the model run, T_Tide (R.Pawlowicz et al, 2002) calculates the tidal current and elevation for the forecast period. The tidal components are then linearly added to the forecast components. For surface currents, wave induced Stokes drifts are added to the model surface current to obtain the total surface current (Tang et al., 2007). The Stokes drift, $\mathbf{u}_s$, is obtained from the 2-dimensional wave spectrum, $E(f, \theta)$, of WW3 by integrations over frequency and direction:

$$\mathbf{u}_s = 4\pi \iint f\mathbf{k}e^{2kz} E(f,\theta)\,df d\theta \tag{6.4}$$

where f is wave frequency, θ is wave direction, $\mathbf{k}$ is wave number and k is the magnitude of $\mathbf{k}$.

There are two options for the Strokes drift in the forecasting system. $\mathbf{u}_s$ can be computed directly from (6.4) at every model grid point. A simpler method is to parameterize $\mathbf{u}_s$ by surface winds :

$$u_s = a\,W + b\,W^2 \tag{6.5}$$

$$\beta = \text{turning angle (positive for clockwise) relative to wind direction} \tag{6.6}$$

where u_s and β are the magnitude and direction of $\mathbf{u}_s$, respectively, and W is 10 m wind speed. The parameters a, b and β are determined from least-squared fits of the Strokes velocities computed from (6.4) for October-December 2007. In most applications (e.g., surface drifter, floating object), vertically averaged surface currents are required. The Stokes velocities in (6.5) and (6.6) are replaced vertically averaged Stokes velocities. The results of the least-squared fits are given in Table 6.4 for different depths of averaging.

Table 6.4. Parameters values of the Stokes drift for different depths of averaging.

Depth (m)	1000*a	1000*b	β(deg)
1	2.525	0.641	3.80
2	1.656	0.533	4.00
3	1.176	0.459	4.10
4	0.889	0.405	4.30
5	0.699	0.363	4.40

Drift tracks are calculated from the total surface current field. Each track starts at a model grid point and is advected by the surface current. Horizontal linear interpolation is used to calculate the surface current field between grid points. Distances are calculated using the plane sailing method which ignores the earth's curvature.

For ice forecasts, all available 1800 UTC ice charts from the previous day are processed and assimilated into the model to correct the model ice field, as described in Section 6.2. For ocean forecasts, 1200 UTC SST data from the previous day are assimilated into the model (Figure 6.6).

6.4 Operational Implementation of WW3

The wave models are implemented on a system of three nested grids (Figures. 6.7, 6.8, 6.9 and Table 6.5). The spatial resolution increases from 1.0° in the coarse grid to 0.5° in the intermediate grid to 0.1667° (10') in the fine resolution grid. This system of grids ensures that energy from distant storms is not lost in simulating storms making landfall in coastal areas of North America. The grid dimensions and resolutions are given in Table 6.5. Etopo2 bathymetry is used from the United States National Geophysical Data Center, at 2 minutes resolution. WW3 is used for the coarse, intermediate and fine resolution simulations. Following the Courant-Friedrichs-Lévy (CFL) stability criterion, the propagation time steps for WW3 are 20 and 10 minutes for the coarse and intermediate grids, respectively, and 4 minute propagation steps for the fine-resolution grid. In Table 6.5, WW3 has 4 time steps: Δt_g is the global time step by which the entire wave model solution is propagated forward in time, $\Delta t_{\rho,1}$ is the maximum spatial (x,y) propagation time step for the lowest frequency, which is required to satisfy the CFL criterion, Δt_{is} is the maximum intra-spectral (k, θ) propagation time step, which is also required to satisfy the CFL criterion, and Δt_{st} is the minimum time step for the integration of the source terms, which is dynamically adjusted for each grid and for Δt_g.

WW3 interpolates the wind fields to the propagation time step of the respective wave model. For fast moving storms, WW3 has a built-in scheme to reduce the source term integration time step when the situation is changing rapidly. Moreover, in WW3 the source term integration time step can be set by the user. Thus, we set the minimum source term time step to 5 minutes in the coarse-resolution grid to adequately simulate the storms considered here. For the intermediate and fine grids, source term time steps were both set to 2.5 (see Table 6.5). Details regarding the spectral range and resolution of the WW3 model are given in Table 6.6, in terms of the lowest and highest frequencies (f_{low} and f_{high}), number of points (n), frequency resolution (Δf) and angular resolutions ($\Delta\theta$). The 48-hour WW3 wave forecasts run twice daily (0000 UTC and 1200UTC).

WW3 simulates waves outside nearshore areas where shallow water wave processes are not important. The model includes standard physics for wave propagation, growth by wind, nonlinear interactions, dissipation due to whitecapping and dissipation due to bottom friction. In coastal, estuary and nearshore areas where water depth is shallow, fine-resolution computational domains are sometimes needed for dedicated studies, nested within coarser–resolution basin-scale domains, in order to resolve complex topography, coastline features, and shallow water wave physics. In these special cases, an option is that the shallow water SWAN wave model (version 40.31) can be applied for a fourth domain, nested within the third domain (Ris et al., 1994; Booij et al., 1996; Booij et al., 1999; Holthuijsen et al. 2003; Booij, 2004) in these specific areas. The physics of SWAN are different from that of WW3, especially for shallow water waves.

SWAN can simulate shoaling, refraction, bottom friction, and depth-induced wave breaking, besides the processes for whitecapping, wind input and nonlinear wave-wave interactions that are present in WW3. SWAN is formulated in terms of an action balance equation. Xu *et al.* (2007) describe the implementation of WW3 and nested grids for the North Atlantic and SWAN for Lunenburg Bay, for studies related to the waves generated by hurricane Juan (September 28-29, 2003).

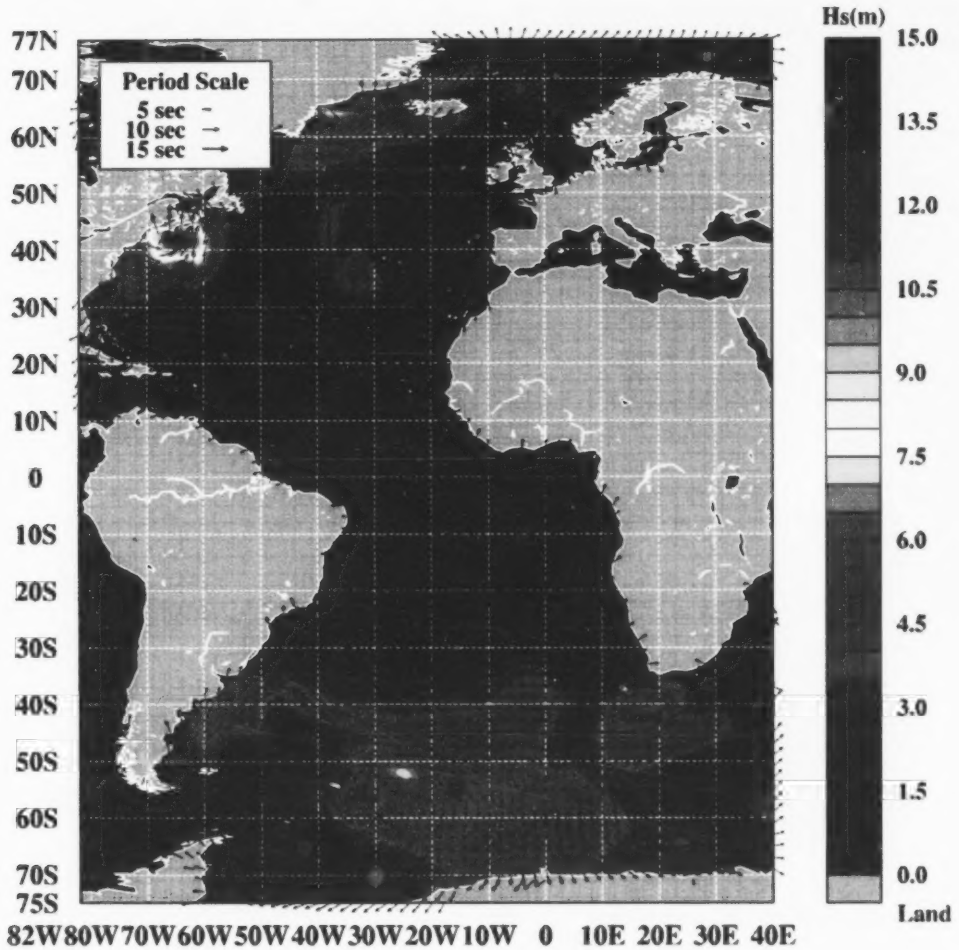

Figure 6.7 Model domain of WW3 - Atlantic Ocean and sample model output (0600 UTC, November 4, 2007). The colors indicate significant wave height. The arrows indicate wave period and direction.

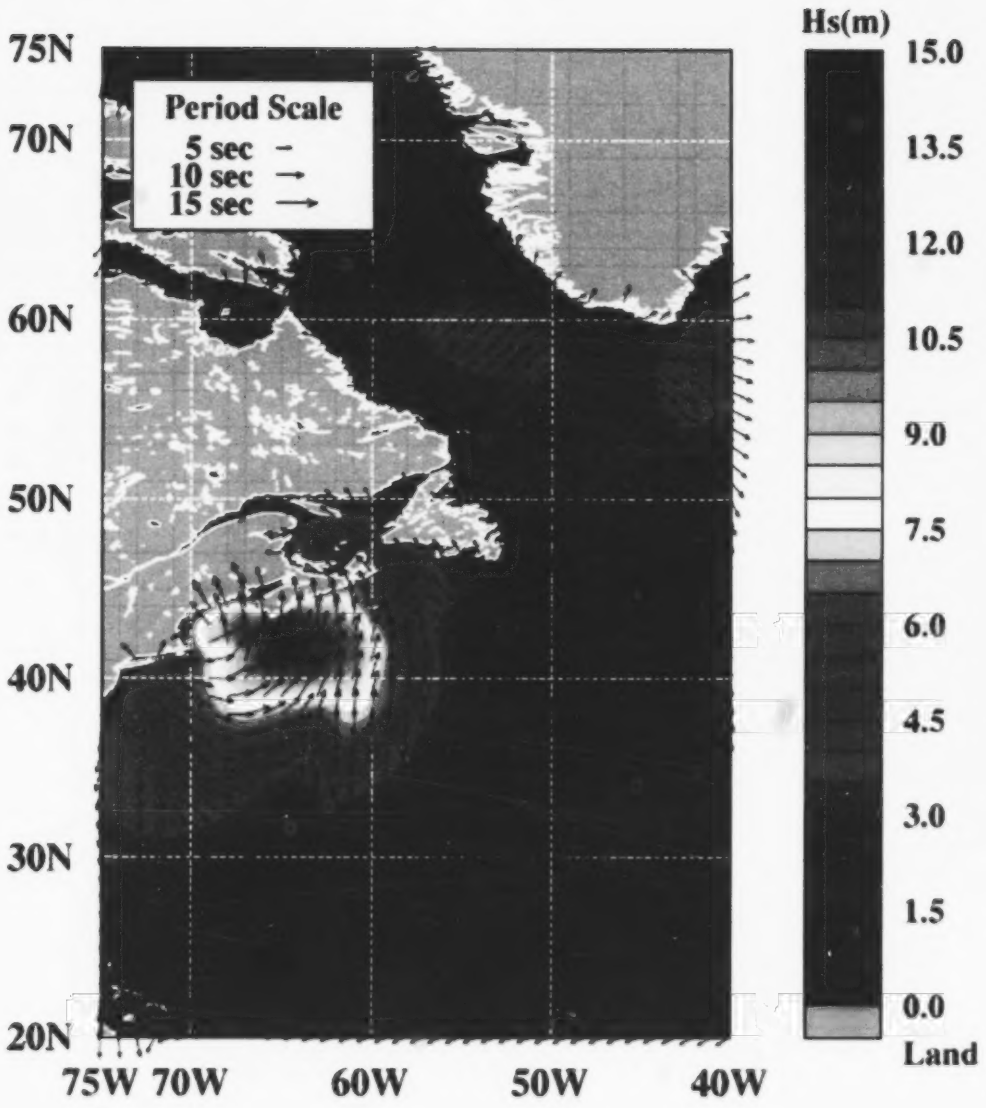

Figure 6.8 Model domain of WW3 – Northwestern North Atlantic Ocean and sample model output (0600 UTC, November 4, 2007). The colors indicate significant wave height. The arrows indicate wave period and direction.

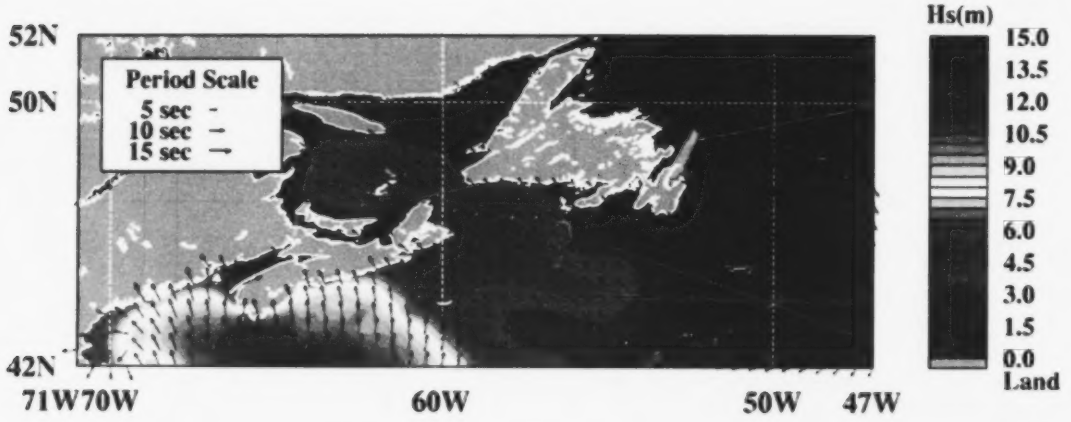

Figure 6.9 Model domain of WW3 – Atlantic maritimes and sample model output (0600 UTC, November 4, 2007). The colors indicate significant wave height. The arrows indicate wave period and direction.

Table 6.5. Geographical location of the grids used in this study: $\Delta_{\lambda,\theta}$ are the resolutions in longitude λ and latitude ϕ, and $N\lambda$ and $N\phi$ are the number of points in λ and ϕ. Finally, Δt is the propagation time step and Δt_{ST} is the required time step for source term integration for the three models, as required to satisfy the CFL criterion.

GRIDS	**Longitude**	**Latitude**	$\Delta_{\lambda,\theta}$	$N\lambda$	$N\phi$	Δt_g	Δt_{ST}
Coarse	40°E – 82°W	75°S– 77°N	1°	123	153	20 min	5.0 min
Intermediate	40°W–75°W	20°N-75°N	0.5°	71	111	10 min	2.min
Fine	47°W–71°W	42°N-52°N	10'	145	61	5 min	2.5 min

Table 6.6. Spectral domains for all models. f_{low}, f_{high} are the default values.

Parameters	**Value**
f_{low}, f_{high} [s^{-1}]	0.0418, 0.6028
nf, Δf	29, $1.1 \times f$
$n\theta$, $\Delta\theta$	36, 10°

References

Battjes, J.A., 1994. Shallow water wave modelling. Proc. Int. Symp. Waves -Phys. Numerical Modelling. University of British Columbia, Vancouver, I, 1-23.

Budyko, M.I., 1974. Climate and Life. Academic Press, New York. 508 pp.

Blanton B., 2005. readgrib. http://www.opnml.unc.edu/OPNML_Matlab/read_grib/read_grib.html

Blumberg, A.F., and G.L. Mellor, 1987. A description of a three-dimensional coastal ocean circulation model, in Three-Dimensional Coastal Ocean Models, *Coastal Estuarine Sci., 4,* edited by N.S. Heaps, pp. 1-16, AGU, Washington, D.C.

Booij, N., L.H. Holthuijsen, and R.C. Ris., 1996. The "SWAN" Wave Model For Shallow Water. *Coastal Engineering, 1*, 668~672.

Booij, N., R.C. Ris and L.H. Holthuijsen, 1999. A third-generation wave model for coastal regions, Part I, Model description and validation, *J. Geophys. Res., 104*, C4, 7649-7666.

Booij, N., 2004: SWAN Cycle III version 40.41 user manual.[Available online at http://fluidmechanics.tudelft.nl/swan/index.htm].

Carton, J.A., G. Chepurin and X. Cao, 2000. A simple ocean data assimilation analysis of the global upper ocean 1950-95, Part I: methodology. *J. Phys. Oceanogr., 30*, 294-309.

Charnock, H., 1955. Wind stress on a water surface. *Quarterly Journal of Royal Meteorological Society, 81*, pp. 639–640.

Clarke, R.A., 1984. Transport through the Cape Farewell-Flemish Cap section, *Rapp. P.V. Reun. Cons. Int. Explor. Mer, 185*, 120-130.

Dunphy, M., F. Dupont, C. G. Hannah, D. Greenberg, 2005. *Validation of a modelling system for tides in the Canadian Arctic Archipelago*. Can. Tech. Rep. Hydrogr. Ocean Sci. 243: vi + 70 pp.

Dunlap, E., B.M. Detracey and C.L. Tang, 2007. Short-wave radiation and sea ice in Baffin Bay. *Atmosphere-Ocean, 45,* 195-210.

Environment Canada, 2005. "MANICE - Manual of Standard Procedures for Observing and Reporting Ice Conditions". http://ice-glaces.ec.gc.ca/ App/WsvPageDsp.cfm?Lang=eng&lnid=23&ScndLvl=no&ID=172

Evans J., 2007. snctools. http://mexcdf.sourceforge.net

Ezer, T. and G.L. Mellor, 1994. Diagnostic and prognostic calculations of the North Atlantic circulation and sea level using a sigma coordinate ocean model. *J. Geophys. Res., 99,* 14159-14171.

Flato, G.M., 1994. McPIC: Documentation for the multi-category particle-in-cell sea ice model. *Can. Tech. Rep. Hydrogr. Ocean Sci., 158.* 74 pp.

Gill, A.E., 1982. Atmosphere-Ocean Dynamics. Academic Press, New York. 662 pp.

Hasselmann, K., T.P. Barnett, E. Bouws, H. Carlson, D.E. Cartwright, K. Enke, J.I. Ewing, H. Gienapp, D.E. Hasselmann, P. Kruseman, A. Meerbrug, P. Müller, D.J. Olbers, K. Richter, W. Sell, and H. Walden, 1973: Measurements of wind-wave growth and swell decay during the Joint North Sea Wave Project (JONSWAP). *Dtsch. Hydrogr. Z., A8*(12), 95 pp.

Hibler, W.D., 1979. A dynamic, thermodynamic sea ice model. *J. Phys. Oceanogr., 9,* 815-846.

Hibler, W.D., 1980. Modeling a variable thickness sea ice cover. *Mon. Wea. Rev., 108,* 1943-1973.

Holthuijsen, L. H., and H.N. Booij, 2003. Phase-decoupled refraction-diffraction for spectral wave models. *Coastal Engineering, 49,* 291-305.

Jerlov, N.G., 1968. Optical Oceanography, 194 pp. Elsevier.

Komen, G. J., L.Cavaleri, M. Donelan, M. Hasselmann, S. Hasselmann, P. A. E. M. Janssen, 1994. Dynamics and Modeling of Ocean Waves. *Cambridge University Press*, 520pp.

Mailhot, J., S. Bélair, L. Lefaivre, B. Bilodeau, M. Desgagné, C. Girard, A. Glazer, A.-M. Leduc, A. Méthot, A. Patoine, A. Plante, A. Rahill, T. Robinson, D. Talbot, A. Tremblay, P. Vaillancourt, A. Zadra, A. Qaddouri, 2006. The 15-km Version of the Canadian Regional Forecast System. *Atmos.-Ocean, 44,* 133-149. DOI 10.3137/ao.440202.

Martinsen, E.A., and H. Engedahl, 1987. Implementation and testing of a lateral boundary scheme as an open boundary condition in a barotropic ocean model. *Coastal Eng., 11,* 603-627.

Mellor, G.L., and A.F. Blumberg, 1985. Modeling vertical and horizontal diffusivities with the sigma coordinate system. *Mon. Wea. Rev., 113,* 1380-1383.

Mellor, G.L., and L.H. Kantha, 1989. An ice-ocean coupled model. *J. Geophys. Res., 94,* 10,937-10,954.

Mellor, G.L. and T. Ezer, 1991. A Gulf Stream model and an altimetry assimilation scheme. *J. Geophys. Res., 96,* 8779-8795.

Mellor, G.L., S. Hakkinen, T. Ezer and R. Patchen, 2002. A generalization of a sigma coordinate ocean model and an intercomparison of model vertical grids, in Ocean Forecasting: Conceptual Basis and Applications, edited by N. Pinardi and J. Woods, pp. 55-72, Springer, Berlin.

Mellor, G.L., and A.F. Blumberg, 2004. Wave breaking and ocean surface layer thermal response. *J. Phys. Oceanogr., 34,* 693-698.

Padilla-Hernãndez, R., W. Perrie, B. Toulany, and P. C. Smith, 2007: Intercomparison of third generation wave models. *Weather and Forecasting* Vol. 22, No. 6.,pages 1229-1242.

Parkinson, C. L., and W. M. Washington, 1979. A large-scale numerical model of sea ice. *J. Geophys. Res., 84,* 311-337.

Paturi, S., G. Han and B. deYoung, 2008. A 3-D multi-constituent, data assimilative tidal model of the northwest Atlantic. *Atmosphere-Ocean.* Submitted.

Paulson, C.L., and J.J. Simpson, 1977. Irradiance measurements in the upper ocean. *J. Phys. Oceangr., 7,* 952-956.

Pawlowicz R., 2006. M_Map. http://www.eos.ubc.ca/~rich

Pawlowicz R., B. Beardsley, and S. Lentz. 2002. *Classical tidal harmonic analysis including error estimates in MATLAB using T_TIDE*, Computers and Geosciences 28, 929-937. http://www.eos.ubc.ca/~rich

Perrie, W., Gunther, H., Rosenthal, W. and Toulany, B., 1989: Modelling wind - generated surface gravity waves using similarity. *Quart. J. Roy. Met. Soc., 115,* 1373-1396.

Ris, R.C., Holthuijsen, L.H. and Booij, N., 1994. A Spectral Model for Waves in the Near shore Zone. *Coastal Engineering, 1,* 68~78.

Semtner, A.J., 1976. A model for the thermodynamic growth of sea ice in numerical investigations of climate. *J. Phys. Oceanogr., 67,* 379-389.

Shine, K.P., 1984. Parameterization of the shortwave flux over high albedo surfaces as a function of cloud thickness and surface albedo. *Q. J .R. Meterol. Soc., 110,* 747-764.

Slørdal, L.H., E.A. Martinsen and A.F. Blumberg, 1994. Modeling the response of an idealized coastal ocean to a traveling storm and to flow over bottom topography. *J. Phys. Oceanogr., 24,* 1698-1705.

Smith, S.D., 1988. Coefficients for sea surface wind stress, heat flux, and wind profiles as a function wind speed and temperature. *J. Geophys. Res., 93,* 15,467-15,472.

Smith, S.D., and F.W. Dobson, 1984. The heat budget at Ocean Weather Station Bravo. *Atmos.-Ocean, 22,* 1-22.

Snyder, R.L., F.W. Dobson, J.A. Elliot, and R.B. Long, 1981: Array measurements of atmospheric pressure fluctuations above surface gravity waves. *J. Fluid Mech.*, **20**, 1166-1174.

Tang, C.L, 2007. High-resolution monthly temperature and salinity climatologies for the northwestern North Atlantic Ocean. *Canadian Data Report of Hydrography and Ocean Sciences,* No. 169: iv + 55 pp.

Tang, C.L., Q. Gui and I. Peterson, 1996a. Modeling the mean circulation of the Labrador Sea and the adjacent shelves. *J. Phys. Oceangr., 26,* 1989-2010.

Tang, C.L. and Q. Gui, 1996b. A dynamical model for wind-driving ice modtion – applicaton to ice drift on the Labrador Shelf. *J Geophys. Res., 101,* 28,343-28,364.

Tang, C.L., C.K. Ross, T. Yao, B. Petrie, B.M. Detracey, and E. Dunlap, 2004. The circulation, water masses and sea ice of Baffin Bay. *Progress of Oceanography, 63,* 183-228.

Tang, C.L., W. Perrie, A.D. Jenkins, B.M. Detracey, Y. Hu, B. Toulany and P.C. Smith, 2007. Observation and modeling of surface currents on the Grand Banks: a study of the wave effects on surface currents. *J. Geophys. Res., 112,* C10025, doi:10.1029/2006JC004028.

Thorndike, A.S., D.A. Rothrock, G.A. Maykut and R. Colony, 1975. The thickness distribution of sea ice. *J. Geophys. Res., 80,* 4501-4513.

Tolman, H. L., 2002. User manual and system documentation of WAVEWATCH-III version 2.22. Technical Note. [Available online at http://polar.ncep.noaa.gov/waves].

Tolman H. L., and Chalikov D.V., 1996. Source terms in a third-generation wind-wave model, *J. Phys. Oceanogr., 26,* 2497-2518.

WAMDI group, 1988. The WAM model – a third generation ocean wave prediction model. *J. Phys. Oceanogr., 18,* 1775-1810.

Xu, F., W. Perrie, B. Toulany, and P. C. Smith, 2007. Wind-generated waves in Hurricane Juan. Ocean Modelling Vol. 16, pages 188–205.

Yao, T., C.L. Tang, and I.K. Peterson, 2000. Modeling the seasonal variation of sea ice in the Labrador Sea with a coupled multi-category ice model and the Princeton Ocean Model. *J. Geophys. Res.*, **105**, 1153-1165.

Yao, T., C.L. Tang, 2003. The formation and maintenance of the North Water. *Atmosphere-Ocean, 41,* 187-201.

Zhang, J., and W.D. Hibler, 1997. On an efficient numerical method for modeling sea ice dynamics. *J. Geophys. Res., 102,* 8691-8702.

Appendix 1. Turbulence closure

This appendix outlines the calculations of the vertical mixing coefficients from turbulence closure. Governing equations for turbulence kinetic energy $q^2/2$ and turbulence macroscale l are

$$\frac{\partial q^2}{\partial t} + u\frac{\partial q^2}{\partial x} + v\frac{\partial q^2}{\partial y} + w\frac{\partial q^2}{\partial z} = \frac{\partial}{\partial z}\left(K_q \frac{\partial q^2}{\partial z}\right) + 2K_M\left[\left(\frac{\partial u}{\partial z}\right)^2 + \left(\frac{\partial v}{\partial z}\right)^2\right] + \frac{2g}{\rho_o}K_H\frac{\partial \rho}{\partial z} - \frac{2q^3}{B_1 l} + \nabla\cdot(A_H\nabla q^2)$$

$$\frac{\partial q^2 l}{\partial t} + u\frac{\partial q^2 l}{\partial x} + v\frac{\partial q^2 l}{\partial y} + w\frac{\partial q^2 l}{\partial z} = \frac{\partial}{\partial z}\left(K_q \frac{\partial q^2 l}{\partial z}\right) + lE_1K_M\left[\left(\frac{\partial u}{\partial z}\right)^2 + \left(\frac{\partial v}{\partial z}\right)^2\right] + \frac{lE_1 g}{\rho_o}K_H\frac{\partial \rho}{\partial z} - \frac{q^3}{B_1}\tilde{w} + \nabla\cdot(A_H\nabla q^2 l)$$

where

$$\tilde{w} = 1 + E_2\left(\frac{l}{\kappa L}\right)^2,$$

$$L^{-1} = (\eta - z)^{-1} + (H + z)^{-1},$$

κ is the von Karman constant and B_1, E_1 and E_2 are empirical constants.

The effects of wave breaking are taken into consideration through the surface boundary condition for q^2. At the surface, the vertical gradient of q^2 is proportional to the cube of the water friction velocity (Mellor and Blumberg, 2004). A consequence of this boundary condition is that the eddy viscosity is non-zero at the surface (Tang *et al.*, 2007). The boundary conditions at the surface are

$$\begin{cases} \dfrac{\partial q^2}{\partial z} = 2\alpha_{BC}u_*^3 & \text{ice free} \\ q^2 = B_1^{2/3}u_*^2 & \text{ice covered} \end{cases}$$

$$q^2 l = 0$$

where α_{BC} is a prescribed constant and u_* is the friction velocity

$u_*^2 = (\tau_{0x}^2 + \tau_{0y}^2)/\rho_0$.

The boundary conditions at the ocean bottom are

$q^2 = B_1^{2/3} u_*^2$

$q^2 l = 0$

where u_* is derived from the bottom stress.

The mixing coefficients K_M, K_H and Kq can be expressed in terms of stability functions S_M, S_H and S_q

$(K_M, K_H, K_q) = lq(S_M, S_H, S_q)$.

The stability functions are derived from the solution of analytic equations (Blumberg and Mellor, 1987) involving the vertical shear and vertical density gradient. In the presence of ice, the mixing coefficient is the average of the values for open ocean and for ice-covered ocean (no wave effects) weighted by ice concentration.

Appendix 2. Generalised sigma coordinates

Generalised sigma coordinates are derived by transforming coordinates (x, y, z, t) to (x^*, y^*, s, t^*). The vertical coordinate s is defined

$$z = s(x^*, y^*, k, t) + \eta(x^*, y^*, t^*) \qquad \text{(A2.1)}$$

where s is a function of the vertical variable k which ranges from 1 at the surface to kb at the ocean bottom. For the purposes of this discussion k is continuous but it is discrete for the computer implementation. Since $\partial z / \partial x = 0$ then

$$0 = \frac{\partial \eta}{\partial x^*} + \frac{\partial s}{\partial x^*} + \frac{\partial s}{\partial k}\frac{\partial k}{\partial x^*}$$

or

$$\frac{\partial k}{\partial x^*} = -\frac{s_{x^*} + \eta_{x^*}}{s_k}.$$

Also, the z derivative of (A2.1) gives

$$\frac{\partial k}{\partial z} = \frac{1}{s_k}.$$

For a function $\phi(x,y,z,t)$, partial derivatives in the old coordinate system are related to partial derivatives in the new coordinate system as

$$\frac{\partial \phi}{\partial x} = \frac{\partial \phi}{\partial x^*} - \frac{\partial \phi}{\partial k}\frac{s_{x^*} + \eta_{x^*}}{s_k}$$

$$\frac{\partial \phi}{\partial y} = \frac{\partial \phi}{\partial y^*} - \frac{\partial \phi}{\partial k}\frac{s_{y^*} + \eta_{y^*}}{s_k}$$

$$\frac{\partial \phi}{\partial z} = \frac{\partial \phi}{\partial k}\frac{1}{s_k}$$

$$\frac{\partial \phi}{\partial t} = \frac{\partial \phi}{\partial t^*} - \frac{\partial \phi}{\partial k}\frac{s_{t^*} + \eta_{t^*}}{s_k}.$$

We define a new vertical velocity ω as

$$w = \omega + s_{t^*} + \eta_{t^*} + u(s_{x^*} + \eta_{x^*}) + v(s_{y^*} + \eta_{y^*}).$$

The continuity equation in transformed coordinates (henceforth dropping the asterisks) is

$$\frac{\partial s_k}{\partial t} + \frac{\partial (u s_k)}{\partial x} + \frac{\partial (v s_k)}{\partial y} + \frac{\partial \omega}{\partial k} = 0. \qquad \text{(A2.2)}$$

The momentum equations in transformed coordinates are

$$\frac{\partial (u s_k)}{\partial t} + \frac{\partial (u^2 s_k)}{\partial x} + \frac{\partial (uv s_k)}{\partial y} + \frac{\partial (\omega u)}{\partial k} - s_k f v = -s_k g(s_x + 2\eta_x)$$
$$+ \frac{s_k g}{\rho_o}\int s_x \frac{\partial \rho}{\partial k}dk - \frac{s_k g}{\rho_o}\int s_k \frac{\partial \rho}{\partial x}dk + \frac{\partial}{\partial k}\left(\frac{K_M}{s_k}\frac{\partial u}{\partial k}\right) + M_x \qquad \text{(A2.3)}$$

$$\frac{\partial (v s_k)}{\partial t} + \frac{\partial (uv s_k)}{\partial x} + \frac{\partial (v^2 s_k)}{\partial y} + \frac{\partial (\omega v)}{\partial k} + s_k f u = -s_k g(s_y + 2\eta_y)$$
$$+ \frac{s_k g}{\rho_o}\int s_y \frac{\partial \rho}{\partial k}dk - \frac{s_k g}{\rho_o}\int s_k \frac{\partial \rho}{\partial y}dk + \frac{\partial}{\partial k}\left(\frac{K_M}{s_k}\frac{\partial v}{\partial k}\right) + M_y \qquad \text{(A2.4)}$$

The heat and salt equations in transformed coordinates are

$$\frac{\partial (T s_k)}{\partial t} + \frac{\partial (u T s_k)}{\partial x} + \frac{\partial (v T s_k)}{\partial y} + \frac{\partial (\omega T)}{\partial k} = \frac{\partial}{\partial k}\left(\frac{K_H}{s_k}\frac{\partial T}{\partial k}\right) + M_T$$

$$\frac{\partial(Ss_k)}{\partial t}+\frac{\partial(uSs_k)}{\partial x}+\frac{\partial(vSs_k)}{\partial y}+\frac{\partial(\omega S)}{\partial k}=\frac{\partial}{\partial k}\left(\frac{K_H}{s_k}\frac{\partial S}{\partial k}\right)+M_S$$

The horizontal mixing terms become

$$M_x=\frac{\partial}{\partial x}\left(2s_kA_M\frac{\partial u}{\partial x}\right)+\frac{\partial}{\partial y}\left[s_kA_M\left(\frac{\partial u}{\partial y}+\frac{\partial v}{\partial x}\right)\right]$$

$$M_y=\frac{\partial}{\partial y}\left(2s_kA_M\frac{\partial v}{\partial y}\right)+\frac{\partial}{\partial x}\left[s_kA_M\left(\frac{\partial u}{\partial y}+\frac{\partial v}{\partial x}\right)\right]$$

$$M_T=\frac{\partial}{\partial x}\left(s_kA_M\frac{\partial T}{\partial x}\right)+\frac{\partial}{\partial y}\left(s_kA_H\frac{\partial T}{\partial y}\right)$$

$$M_S=\frac{\partial}{\partial x}\left(s_kA_M\frac{\partial S}{\partial x}\right)+\frac{\partial}{\partial y}\left(s_kA_H\frac{\partial S}{\partial y}\right)$$

These forms are not simply the transformations of (2.8). This relates to separating vertical mixing from horizontal mixing in a coordinate system in which constant k surfaces are sloping (Mellor and Blumberg, 1985 and Mellor et al., 2002).

Appendix 3. Rotated spherical coordinate system

Coordinates **r** on a unit sphere are transformed to **r′** in a rotated system (4.2) with the matrix **R** by

$$\mathbf{r'}=\mathbf{Rr}=\mathbf{R}_\zeta\mathbf{R}_\eta\mathbf{R}_\xi\mathbf{r} \qquad \text{(A3.1)}$$

where $\mathbf{R}_\xi$, $\mathbf{R}_\eta$, $\mathbf{R}_\zeta$ are transformation matrices for rotations by the individual angles ξ, η, and ζ respectively (Figure 4.2).

The individual rotation matrices are

$$\mathbf{R}_\xi=\begin{pmatrix}\cos\xi & \sin\xi & 0\\ -\sin\xi & \cos\xi & 0\\ 0 & 0 & 1\end{pmatrix},\quad \mathbf{R}_\eta=\begin{pmatrix}\cos\eta & 0 & -\sin\eta\\ 0 & 1 & 0\\ \sin\eta & 0 & \cos\eta\end{pmatrix},\quad \mathbf{R}_\zeta=\begin{pmatrix}\cos\zeta & \sin\zeta & 0\\ -\sin\zeta & \cos\zeta & 0\\ 0 & 0 & 1\end{pmatrix} \qquad \text{(A3.2)}$$

giving the matrix **R** as

$$\begin{pmatrix} \cos\varsigma\cos\eta\cos\xi - \sin\varsigma\sin\xi & \cos\varsigma\cos\eta\sin\xi + \sin\varsigma\cos\xi & -\cos\varsigma\sin\eta \\ -\sin\varsigma\cos\eta\cos\xi - \cos\varsigma\sin\xi & -\sin\varsigma\cos\eta\sin\xi + \cos\varsigma\cos\xi & \sin\varsigma\sin\eta \\ \sin\eta\cos\xi & \sin\eta\sin\xi & \cos\eta \end{pmatrix}. \tag{A3.3}$$

As well as transforming coordinates, it is also necessary to transform components of vectors tangent to the sphere. Define $\alpha(\phi,\theta)$ as the angle between parallels of latitude (Figure A3.1). The angle between a vector and the local parallel in the rotated system is the corresponding angle in the original system minus α. Denoting longitude and co-latitude in the rotated coordinate system as (ϕ',θ'), then

$$\tan\alpha = \frac{-\partial\theta/\partial\phi'}{\partial\phi/\partial\phi'\sin\theta}\ . \tag{A3.4}$$

From (4.1) (ϕ, θ) are related to (x, y, z) by

$$\tan\phi = y/x$$

$$\cos\theta = z. \tag{A3.5}$$

The partial derivatives in (A3.4) may be written as

$$\frac{\partial\theta}{\partial\phi'} = \frac{\partial}{\partial\phi'}\cos^{-1}z = -\frac{\partial z/\partial\phi'}{\left(1-z^2\right)^{1/2}} \tag{A3.6}$$

and

$$\frac{\partial\phi}{\partial\phi'} = \frac{\partial}{\partial\phi'}\tan^{-1}(y/x) = \frac{1}{x^2+y^2}\left(x\frac{\partial y}{\partial\phi'} - y\frac{\partial x}{\partial\phi'}\right). \tag{A3.7}$$

Eqs. (A3.6) and (A3.7) involve derivatives $\partial\mathbf{r}/\partial\phi'$. From (A3.1)

$$\begin{pmatrix} x \\ y \\ z \end{pmatrix} = \mathbf{R}^{-1}\begin{pmatrix} x' \\ y' \\ z' \end{pmatrix} = \mathbf{R}^{-1}\begin{pmatrix} \sin\theta'\cos\phi' \\ \sin\theta'\sin\phi' \\ \cos\theta' \end{pmatrix}. \tag{A3.8}$$

The partial derivatives in (A3.6) and (A3.7) are then

$$\begin{pmatrix} \partial x/\partial\phi' \\ \partial y/\partial\phi' \\ \partial z/\partial\phi' \end{pmatrix} = \mathbf{R}^{-1}\begin{pmatrix} -\sin\theta'\sin\phi' \\ \sin\theta'\cos\phi' \\ 0 \end{pmatrix}. \tag{A3.9}$$

We obtain α by substituting (A3.9) into (A3.6) and (A3.7) and then substituting (A3.6) and (A3.7) into (A3.4).

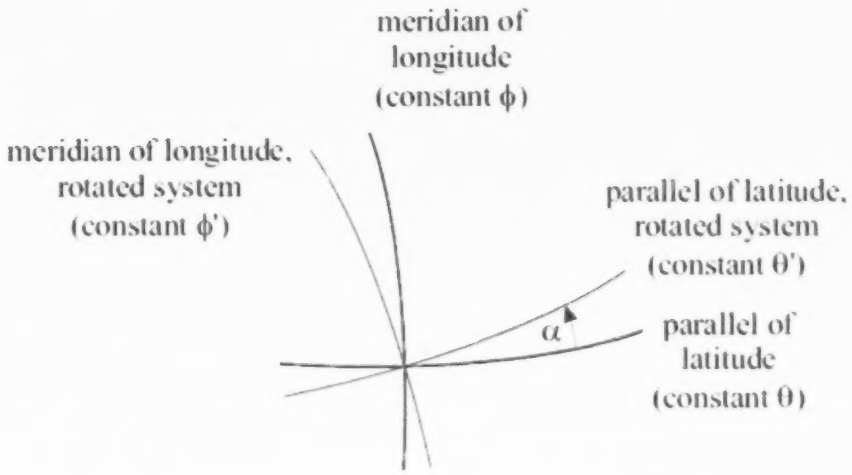

Figure A3.1: The angle α between a parallel of latitude in the rotated coordinate system and a parallel of latitude in the original system enables the transformation of components of a vector.

Appendix 4. Two-dimensional statistical interpolation

Consider a variable T_i at a model time and grid point denoted by the subscript i. The model value T_i^m is corrected by past or present observations to yield an assimilated value, T_i^a, according to

$$T_i^a = T_i^m + \sum_{\alpha=1}^{N} P_{i\alpha}(T_\alpha^o - T_\alpha^m) \qquad \text{(A4-1)}$$

where T_α^o is the observation and T_α^m is the model value at the time and location of the observation denoted by the subscript "α". N is the number of observations to be included in the assimilation. $P_{i\alpha}$ are weights obtained by minimizing the difference between the model prediction and the observation, which are solutions of the following algebraic equations (Mellor and Ezer, 1991):

$$\sum_{\alpha=1}^{N} P_{i\alpha}(M_{\alpha\beta} + D_{\alpha\beta}) = M_{i\beta} \qquad \beta = 1,2,\ldots\ldots,N \qquad \text{(A4-2)}$$

where $M_{\alpha\beta}$ and $D_{\alpha\beta}$ are the error matrices for model and observation, respectively:

$$M_{\alpha\beta} = \left\langle \Delta T_\alpha^m \cdot \Delta T_\beta^m \right\rangle \qquad D_{\alpha\beta} = \left\langle \Delta T_\alpha^o \cdot \Delta T_\beta^o \right\rangle. \tag{A4-3}$$

ΔT_α^m and ΔT_α^o are the model and observation errors, respectively. The error matrices can be parameterized by a Gaussian and a delta function (Mellor and Ezer, 1991; Carton *et al.*, 2000):

$$M_{\alpha\beta} = \varepsilon_m^2 \exp\left[-\frac{(x_\alpha - x_\beta)^2}{2L_x^2} - \frac{(y_\alpha - y_\beta)^2}{2L_y^2} - \frac{(t_\alpha - t_\beta)^2}{2\tau_x^2} \right] \tag{A4-4}$$

$$D_{\alpha\beta} = \varepsilon_o^2 \delta_{\alpha\beta} \tag{A4-5}$$

where L_x, L_y and τ are the correlation scales of the model errors. If the horizontal correlation scale is much larger than the grid spacing of the model, the spatial part of (A4-4) can be neglected, and (A4-1) is reduced to:

$$T_i^a = T_i^m + \frac{\varepsilon_m^2}{\varepsilon_m^2 + \varepsilon_o^2} \exp\left[-\frac{(t_i - t_1)^2}{2\tau^2} \right] (T_1^o - T_1^m) \tag{A4-6}$$

where the subscript "1" denotes the time of the most recent observation ($t_1 \le t_i$).